

Accretion of clumpy cold gas onto massive black holes binaries: the challenging formation of extended circumbinary structures

Cristián Maureira-Fredes^{1*}, Felipe G. Goicovic^{2,3}, Pau Amaro-Seoane^{4,5,6,7} and Alberto Sesana⁸

¹Max Planck Institute for Gravitational Physics (Albert Einstein Institute), Am Mühlenberg 1, 14476, Potsdam-Golm, Germany

²Heidelberg Institute for Theoretical Studies (HITS), Schloss-Wolfsbrunnengasse 35, D-69118 Heidelberg, Germany

³Instituto de Astrofísica, Pontificia Universidad Católica de Chile, Av. Vicuña Mackenna 4860, 7820436 Macul, Santiago, Chile

⁴Institute of Space Sciences (ICE, CSIC) & Institut d'Estudis Espacials de Catalunya (IEEC)

at Campus UAB, Carrer de Can Magrans s/n 08193 Barcelona, Spain

⁵Institute of Applied Mathematics, Academy of Mathematics and Systems Science, CAS, Beijing 100190, China

⁶Kavli Institute for Astronomy and Astrophysics, Beijing 100871, China

⁷Zentrum für Astronomie und Astrophysik, TU Berlin, Hardenbergstraße 36, 10623 Berlin, Germany

⁸School of Physics and Astronomy, University of Birmingham, Edgbaston, Birmingham B15 2TT, United Kingdom

22 January 2018

ABSTRACT

Massive black hole binaries (MBHBs) represent an unavoidable outcome of hierarchical galaxy formation, but their dynamical evolution at sub-parsec scales is poorly understood, due to a combination of uncertainties in theoretical models and lack of firm observational evidence. In gas rich environments, it has been shown that the presence of a putative extended, steady circumbinary gaseous disc plays an important role in the MBHB evolution, facilitating its coalescence. How gas on galactic scales is transported to the nuclear region to form and maintain such a stable structure is, however, unclear. One possibility is that, following the violent merger dynamics, turbulent gas condenses in cold clumps and filaments that are randomly scattered towards the nucleus. In this scenario, gas is naturally transported on parsec scales and interacts with the MBHB in discrete incoherent pockets. The aim of this work is to investigate the gaseous structures arising from this interaction. We employ a suite of smoothed-particle-hydrodynamic simulations to study the formation and evolution of gaseous structures around a MBHB constantly perturbed by the incoherent infall of molecular clouds. We investigate the influence of the infall rate and angular momentum distribution of the clouds on the geometry and stability of the arising structures. We find that the continuous supply of incoherent clouds is a double-edge sword, resulting in the intermittent formation and disruption of circumbinary structures. Anisotropic cloud distributions featuring an excess of co-rotating events tend to generate more prominent co-rotating circumbinary discs. Similar structures are also seen when mostly counter-rotating clouds are fed to the binary, even though they tend to be more compact and less stable. In general, our simulations do not show the formation of extended smooth and stable circumbinary discs, typically assumed in analytical and numerical investigations of the the long term evolution of MBHBs.

Key words: accretion – circumbinary discs – hydrodynamics – galaxies: evolution – galaxies:nuclei

1 INTRODUCTION

Thanks to advances in high angular resolution instrumentation, our understanding of the central regions in galaxies has gone through a major breakthrough. Space-borne telescopes such as the Hubble Space Telescope and adaptive optics from the ground allow us

to investigate the kinematics and distribution of gas and stars at sub-parsec scales for external galaxies (see e.g. Kormendy 2003; Kormendy & Ho 2013) and to milli-pc for the Milky Way (see e.g. Schödel et al. 2003, 2014; Gallego-Cano et al. 2017; Schödel et al. 2017 and, in particular, the review of Genzel et al. 2010). A capital conclusion is that massive dark compact objects, very likely massive black holes (MBH), with a mass typically ranging between $10^{6-9} M_{\odot}$ are lurking at the innermost centre of most large galaxies

* E-mail: cmaureirafredes@gmail.com

in the observable range. Moreover, the formation and evolution of these objects and their host galaxies seem to be linked (Magorrian et al. 1998; Ferrarese & Merritt 2000; Gebhardt et al. 2000; Häring & Rix 2004).

On the other hand, from a theoretical standpoint hierarchical models best explain the formation of structures in the Universe, down to the size of a galaxy. This implies that galaxies, during their lifetime, have suffered at least one merger, if not several (see e.g. Volonteri et al. 2003, for hierarchical merger studies in Λ CDM Cosmology). If these galaxies harbour a MBH in their centre, during the collision they will sink to the centre of the merged galaxy, form a binary and shrink its semi-major axis and become “harder” thanks to the interaction with stars coming from the surrounding stellar system in which they are embedded (see e.g. Begelman et al. 1980; Quinlan 1996; Sesana et al. 2007; Colpi & Dotti 2011). A star will strongly interact with the binary of MBHs by removing energy and angular momentum out of it, so that it will be re-ejected into the stellar system with a higher kinetic energy, and the semi-major axis of the binary will shrink a bit more. Nevertheless, the loss-cone (see e.g. Frank & Rees 1976; Amaro-Seoane et al. 2004), which provides the MBH binary (MBHB) with stars to interact with, is soon empty, halting the evolution of the binary. The pace of subsequent shrink of the MBHB is dictated by the rate at which new stars are scattered into the loss cone. For spherical stellar distributions, the relevant scale is set by the two-body scattering timescale, that can exceed the Hubble time (Milosavljević & Merritt 2001). When this happens, the binary stalls: the MBHs are still bound but they will not coalesce in a Hubble time. They are emitting gravitational waves, but the energy loss is too weak.

This situation is known as “the last parsec problem”, because the separation between the MBHs is typically of the order of ~ 1 pc (Begelman et al. 1980; Milosavljević & Merritt 2003; Merritt & Milosavljević 2005). Whether or not these binaries will merge in a Hubble time is a question that depends on various issues and is currently debated. However, the emerging consensus is that such binaries will in most of the cases overcome this hang-up, due to efficient loss cone re-population in the triaxial, dynamically un-relaxed stellar distribution produced by galaxy mergers (Berczik et al. 2006; Preto et al. 2011; Khan et al. 2011; Vasiliev et al. 2015; Sesana & Khan 2015). MBHBs will therefore get to the phase in their evolution in which they efficiently emit gravitational waves to be detected with a GW observatory such as the Laser Interferometer Space Antenna (LISA, see Amaro-Seoane et al. 2017a, 2013a, 2012).

In gas rich galaxies, which become dominant at low galaxy masses and/or high redshifts, a key factor to surmount this last stretch is the role of the gas, which may be crucial in the evolution of the binary (Escala et al. 2004, 2005a). For instance, the work of Cuadra et al. (2009) found that gaseous discs should commonly help in the merger of MBHs with masses of interest for LISA, whilst this mechanism fails for masses larger than $\sim 10^7 M_\odot$.

The evolution of MBHBs interacting with a circumbinary gaseous structure has been investigated by a number of authors. In most studies, gas is assumed to be distributed in a steady, extended circumbinary disc that is either co-rotating (see e.g. Armitage & Natarajan 2005; Cuadra et al. 2009; Haiman et al. 2009; Kocsis et al. 2012a; Amaro-Seoane et al. 2013b; D’Orazio et al. 2013a; Tang et al. 2017a) or a counter-rotating (see e.g. Roedig & Sesana 2014; Nixon & Lubow 2015; Amaro-Seoane et al. 2016) with respect to the rotation of the MBHB. The binary-disc system is assumed to evolve in isolation, and almost

no attempt has been made to connect the system with the larger scale galactic environment that is providing the mass supply to the gaseous structure. The violent interaction of two merging, gas rich galaxies is expected to produce a turbulent environment in which cold clumps and filaments of gas continuously interact exchanging angular momentum and eventually infalling toward the centre of the merger remnant. The initial orbit of the galaxy merger provides a large source of angular momentum, the geometry and angular momentum distribution of the infalling matter is therefore set by the competing effect of ordered dynamics due to the large scale rotation of the merger remnant and chaotic motions driven by turbulence and clumps and filament scattering (Sesana et al. 2014).

It has been proposed that accretion of gas on to the binary can happen either (i) in a coherent way, so that the angular momentum direction is basically kept constant through all the episodes of accretion (Dotti et al. 2010), (ii) stochastically, meaning that the gas accretes on to the black holes in randomly oriented planes (King et al. 2005a; King & Pringle 2006), for which we have observational evidences, such as in the nucleus of the Abell 2597 galaxy cluster (Tremblay et al. 2016) or in the AGN PKS B1718-649 (Maccagni et al. 2018). Cold chaotic accretion has been linked to several physical mechanisms acting on the interstellar medium, such as turbulence, rotation, AGN/Supernovae feedback, among others (Hobbs et al. 2011; Gaspari et al. 2013, 2015, 2017). Also, it has been pointed that (iii) actually accretion might be a mixture of both, coherent and stochastic accretion, with different degrees of anisotropy, as investigated by Dotti et al. (2013) to address possible anisotropies present in the gas in the nuclear regions of active galaxies.

Accretion on to a MBHB of single clouds has been investigated numerically by Dunhill et al. (2014), Goicovic et al. (2016) and Goicovic et al. (2017), taking into account different orbital configurations and cooling rates. The authors found that the interaction prompts a transient phase of high accretion onto the MBHB, while part of the leftover gas settles into a circumbinary disc of various masses and sizes depending on the initial orbit of the cloud. Whether such gaseous structure can be kept stable and grow in time under the influence of a series of episodic accretion events is unclear, as the successive infall of various clouds on to a MBHB has not been addressed yet. In this article, we present for the first time to our knowledge dedicated, detailed numerical simulations of repeated gaseous infall episodes and accretion on to a MBHB in a post-merger galactic nucleus to assess the architecture of the gas forming around the binary. We consider stochastic feeding of the binary, assuming different degrees of anisotropy in the distribution of the infalling clouds, as well as different feeding rates.

The paper is organised as follows. In §2 we describe the main technical features of the simulation, focusing on physical ingredients and numerical details that have been developed specifically for this suite of simulations. In §3 we define the initial conditions of each individual run, providing all the cloud parameter details necessary to reproduce our runs. We test the stability and convergence of our numerical scheme against critical parameters such as the assumed sink radius and the number of particles used to simulate each cloud in §4. The results of all simulations, including an extensive description of the transient and long term circumbinary structures, and individual mini-discs are presented in §5 and the significance of our main finding and future outlook are discussed in §6. The impact on the evolution of the binary itself is presented in a companion paper, Goicovic et al. (2018).

Additional data and multimedia material of Goicovic et al.

(2018) and the current publication can be found in the website of the project ¹.

2 METHODS

We study the evolution of the MBH-clouds system using GADGET-3, a Smooth Particle Hydrodynamics (SPH) and N -body code, which is a modified version of GADGET-2 ². Every particle is represented as a point-mass, characterised by its 3-D position and velocity, and the code solves for the hydro-dynamical and gravitational interaction of the elements, which are organised in a tree structure (Barnes & Hut 1986).

Specific to our implementation is the modelling of the MBHB as two equal-mass sink particles, initialised in a Keplerian circular orbit with centre of mass at rest in the origin of our Cartesian reference frame. We established the code units such as the initial semi-major axis, orbital period and mass of the black hole binary are equal to one, i.e. $a_0 = P_0 = M_0 = 1$ ³, which can be re-scaled to an astrophysical system as detailed in Goicovic et al. (2016). Along the paper, we will present results for a physical MBHB with initial semi-major axis of $a = 0.2\text{pc}$, a total initial mass of $M_{\text{bin}} = 10^6 M_\odot$, and an orbital period of $P = 8400\text{ yr}$. We will refer to this astrophysical rescaling as our *fiducial system*.

Each infalling molecular cloud is modelled as a spherical distribution of equal-mass SPH particles. Each cloud has a mass of $M_c = 0.01 M_0$ and, to verify the convergence of our simulations, is modelled with increasing resolution, using four different number of particles

- $N_c = 5 \times 10^4$ (50k, default simulation value),
- $N_c = 2 \times 10^5$ (200k),
- $N_c = 5 \times 10^5$ (500k),
- $N_c = 1 \times 10^6$ (1m).

The main configuration of our simulation set-up is described in Goicovic et al. (2016) and visualised in Figure 1. It is an adaptation of the scheme presented in Bonnell & Rice (2008), in which we:

- replace the central black hole by a MBHB;
- set the initial separation between the cloud and the MBHB to 15 (in code units, corresponding to 3 pc rescaled to our fiducial system);
- adopt an initial velocity modulus of the cloud of $v_c = 0.5 v_0 = 0.5 \sqrt{GM_0/a_0}$;
- gauge the encounter impact parameter by varying the θ_{vel} angle formed by the cloud velocity vector with the direction connecting the centre of masses of the cloud and of the MBHB.

In the top panels of figure 1, we sketch the set up of a co-rotating and a counter-rotating encounter. In the first case, the angular momentum vector of the cloud orbit, \vec{L}_c , is aligned with the orbital angular momentum vector of the MBHB, \vec{L}_{bin} ; in the latter, the two angular momenta have opposite direction. In general, the two angular momenta can have arbitrary relative orientation. In our set-up, we fix the reference frame so that the MBHB is initially at rest in the origin and \vec{L}_{bin} is along the positive z axis. We then

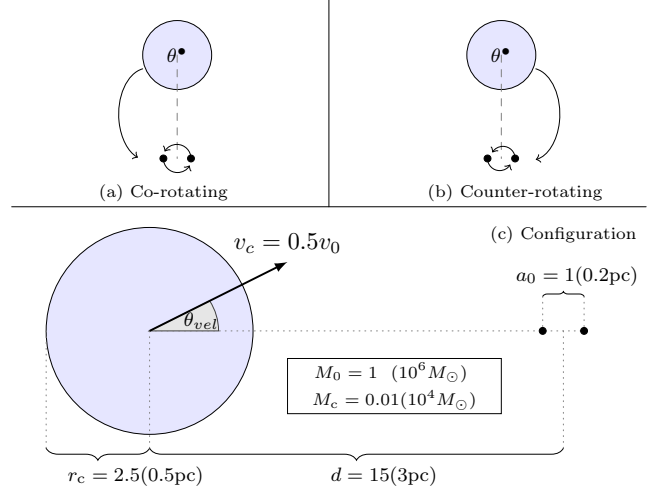


Figure 1. Schematic representation of selected configurations of the simulations: (a) Co-rotating case, the gas cloud infalls following the MBHB orbit; (b) Counter-rotating case, the gas cloud infalls oppositely to the MBHB orbit. Panel (c) sketches how the cloud impact parameter is tuned by changing the angle θ_{vel} (see description in main text). The parameters of the system (initial separation between the cloud and MBHB, initial cloud velocity, masses and sizes of both the cloud and the MBHB) are listed in the figure.

generally refer to a cloud as “co-rotating” (“counter-rotating”) if the z component of its \vec{L}_c is aligned (counter-aligned) to \vec{L}_{bin} .

When added to the simulation, the cloud is composed by spherically distributed particles with uniform density, sustained against gravitational collapse by a turbulent internal velocity field. We set up this turbulence by drawing from a Gaussian random distribution with a power spectrum $P_v(k) \propto k^{-4}$, where k is the wave-number of the velocity perturbation in Fourier space. This distribution is chosen to match the observed velocity of molecular clouds (Larson 1981).

2.1 Additional physics

2.1.1 Accretion

Each MBH in the simulation is represented by a sink particle, which means that it will accrete any particle entering a pre-defined sink radius, but otherwise it interacts only gravitationally with other SPH particles. We do not use the built-in stochastic accretion model that is included in GADGET, which is not appropriate for the problem in hand, where a reliable accretion procedure for individual gas particles, beyond a stochastic selection scheme, is required. Entering the sink-radius must be a necessary but not sufficient condition for accretion. In fact physically unbound particles can simply fly-by across the sink radius. Therefore, to avoid spurious accretion, we verify that each candidate particle entering the sink radius is bound to the associated MBH. In practice, a gas particle will be accreted if the following conditions are satisfied:

$$r_{\text{gas}} \leq r_{\text{sink}} \quad (1)$$

$$E_{\text{bind}} < 0 \quad (2)$$

where r_{gas} is the relative distance between the MBH and gas

¹ <http://multipleclouds.xyz/>

² <http://wwwmpa.mpa-garching.mpg.de/galform/gadget/>

³ Throughout the paper the subscript $_0$ will refer to initial system parameters.

particle, and we take a fiducial $r_{\text{sink}} = 0.1$ which is a 10% of the initial separation of the MBHB. A convergence study of the results against the chosen value of r_{sink} is presented in §4.1. In order to be able to verify angular momentum conservation, it is important to keep track of the accreted gas particles. The positions and velocity of those particles at the moment of accretion are locally stored, to be used in the computation of the angular momentum of the system when required.

2.1.2 Thermodynamics

The thermodynamics of the gas is modelled using a barotropic equation of state (Bonnell 1994; Escala et al. 2005b; Dotti et al. 2006),

$$P = K\rho^\gamma, \quad (3)$$

where the constant γ depends on the gas density. The value of K represents the entropic function of each gas particle in the code (Springel & Hernquist 2002), and because it depends explicitly of γ , it must be calculated so that the pressure behaves as a continuous function of density. We choose an effective equation of state that represents the behaviour of a collapsing protostellar cloud, whereby the low density gas evolve isothermally up to some critical density (ρ_c), at which point it becomes adiabatic (Bate et al. 1995). This can be represented as:

$$\gamma = 1.0 \quad \text{for } \rho \leq \rho_c; \quad (4)$$

$$\gamma = 1.4 \quad \text{for } \rho > \rho_c \quad (5)$$

As explained in Goicovic et al. (2016), the addition of these two regimes breaks the scale-free nature of our simulations, although the results can be scaled within a certain range of critical densities, as explained in Goicovic et al. (2016).

For the simulations presented in this paper we choose $\rho_c = 10^{-2} M_0 a_0^{-3}$ in code units, corresponding to $10^{-16} \text{ g cm}^{-3} \approx 1.5 \times 10^6 M_\odot \text{ pc}^{-3}$ when scaled to our fiducial system. Note that this is two orders of magnitude smaller than the value adopted in Goicovic et al. (2016). This modification was introduced to save computational cost, as some of the configurations produce a large number of gas clumps. Evolving these high density regions requires very small time-steps. Hence, by effectively stopping the collapse at much lower densities, this modification prevents simulations from stalling due to excessively small time-steps.

With this approach we are mimicking the evolution of a multi-phase gas without implementing sophisticated cooling mechanisms or radiative transfer schemes. The isothermal treatment of the gas is qualitatively representative of optically thin media, where cooling is very efficient. Since our goal is to study the dynamics of the gas and not the detailed thermodynamic evolution of the dense regions, this treatment suites our purposes. Because the gas dynamics is mostly dominated by the gravitational potential generated by the binary, we do not expect the thermodynamics to have a major impact in our results. Nevertheless, future studies should include a proper thermodynamic treatment of the gas.

2.1.3 External potential

MBHBs live in the dense environment of galactic nuclei, sitting at the bottom of the galactic potential well. Although this potential does not significantly affect the cloud-MBHB individual

interaction, it is important to take it into account when performing an extensive experiment including the interaction of multiple clouds. In fact, the external potential is relevant in two ways:

- it changes the dynamics of the gas flung away by the binary, keeping it bound to the system and allowing it to come back for further interactions;
- it acts as a restoring force, keeping the binary close to the origin of the reference frame (i.e. to the bottom of the potential well).

In practice the inclusion of the potential does not greatly affect the dynamics of the close MBHB-cloud encounters – which remains dominated by the gravity exerted by the MBHB – and it ensures angular momentum and energy conservation due to its spherically symmetric nature. Most importantly, it avoids drifting of the system away from the coordinate origin, which is problematic when clouds are added to the system at different times. Instead, the MBHB experiences a gentle wandering with no secular effects 4 and, together with its surrounded gas structures, is kept close to the reference frame origin.

To determine the potential, we assume that matter is distributed around the origin following an Hernquist density profile (Hernquist 1990):

$$\rho(r) = \frac{M_*}{2\pi} \frac{a_*}{r} \frac{1}{(r + a_*)^3}, \quad (6)$$

which implies a cumulative mass distribution given by

$$m_*(r) = M_* \frac{r^2}{(r + a_*)^2}, \quad (7)$$

where M_* and a_* are the total mass and scale radius of the distribution. Based on our fiducial system where $M_{\text{bin}} = 10^6 M_\odot$, we derived M_* by assuming the hole to bulge mass relation of Magorrian et al. (1998) and we computed the scale radius using the radius to stellar mass relation of Dabringhausen et al. (2008). In code units, this gives

- $M_* = 4.78 \times 10^2 M_0$,
- $a_* = 3.24 \times 10^2 a_0$,

which implies $m_*(< a_0) \approx 5 \times 10^{-3} M_0$, thus a negligible effect on the Keplerian nature of the MBHB.

2.2 Other technical adjustments and numerical calibration

2.2.1 Dynamics of the sink particles

The simple inclusion of dynamical ‘sinks’ several order of magnitude more massive than the other SPH particles, introduced a number of issues with the SPH scheme. This was already noticed in Cuadra et al. (2009), who proposed to extract the sink particles from the tree for a better integration of their trajectories. We adopted the same strategy here, integrating the MBHB orbit with a fixed time step $\Delta T = 0.02 P_0$, thus allowing the binary positions and velocities to be updated more often than typical SPH particles. We verified that this made the evolution more reliable, ensuring that no crucial interactions between particles and the MBHBs were missed along the integration.

Still, close inspection of the MBHB evolution showed unphysical jumps in the angular momentum of the system. We verified that this was related to the frequency of update of the SPH

tree. In SPH simulations one can choose how often the particle tree (that defines how particles are grouped in computing mutual forces) is generated and updated, which can be controlled by an adjustable parameter in GADGET. So long as the system does not experience dramatic changes, simulations run smoothly with sparse tree updates. However, we are dealing here with multiple clouds infalling onto a MBHB from different directions, triggering violent episodes of accretion, which is clearly not the standard system handled by SPH codes of this type. We found that this required reconstructing the tree 100 times more often than in the default GADGET configuration.

2.2.2 Injection of clouds

At the beginning of each simulation, only one cloud is present in the system besides the MBHB. All the following clouds interact with the binary at later times and therefore need to be included into the system ‘on the fly’. Once the injection time for the new cloud is reached, the simulation is stopped and the new cloud is added. Each cloud is characterised by a specific set of ids, so that particles can always be tracked back to their original cloud. This is useful to track the relative importance of each cloud in the accretion process, or in the formation of specific circumbinary structures. Once the cloud is added, the simulation is resumed and the integrator can adapt to the new particles, forming the tree again, and handling this new scenario. The procedure is repeated for each cloud. Note that due to the inclusion of new clouds, the total angular momentum is not conserved. The angular momentum of each injected cloud is, however, known, and it is therefore easy to track angular momentum conservation along the integration of the system.

With the exception of the ones accreted by the MBHB, we do not remove any particle from the simulation. In fact, because of the way the tree is constructed, particles that are flung far away from the binary are grouped in large structures and integrated rarely, representing a negligible contribution to the computational burden. Moreover, the addition of the external potential keeps the structure compact, minimising the number of particles escaping at distances larger than $100a_0$.

2.2.3 Softening and sink radius

Finally it is important the selection of appropriate softening parameter. We choose for the sink particles a value of $\epsilon_{\text{BH}} = 0.01a_0 = 0.002\text{pc}$, and for SPH particles $\epsilon_{\text{gas}} = 0.001a_0 = 0.0002\text{pc}$. These values are small enough to ensure we are not bypassing gravitational interactions, and are an order or magnitude smaller than the maximum value recommended by [Bonnell & Rice \(2008\)](#). As mentioned above, we fix the sink radius at $r_{\text{sink}} = 0.1a_0$. We performed (see §2.2.1) a series of tests ensuring that neither the dynamics of the MBHB nor the accretion of SPH particles is sensitive to the specific choice of r_{sink} .

3 INITIAL CONDITIONS AND RUN DESCRIPTION

In the previous Section, we defined the main physical ingredients and technical features of our simulations, we now proceed in detailing the initial conditions of our set of runs. Our goal is to simulate a series of clouds interacting with a central MBHB sitting at the bottom of a fixed potential well. The MBHB is initially in the coordinate frame origin and has a separation $a_0 = 1$ in code

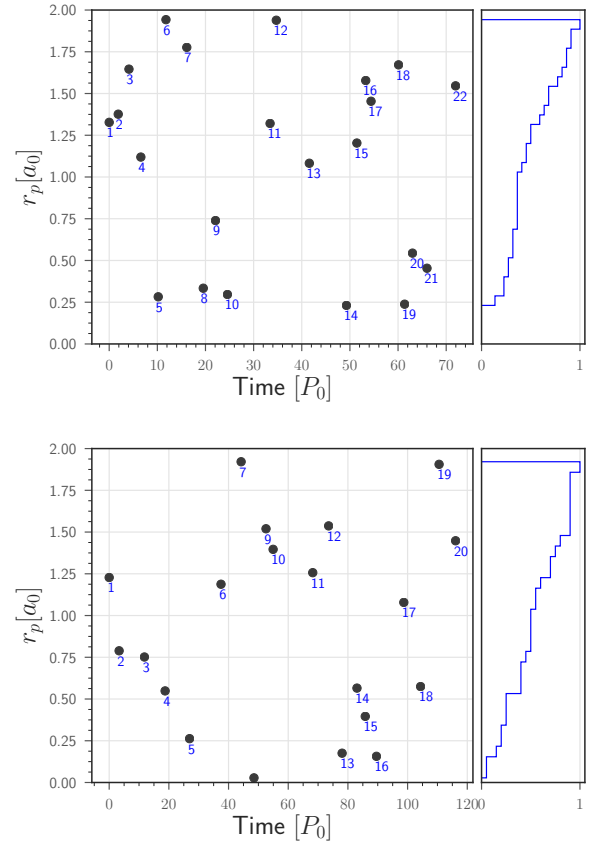


Figure 2. Pericentre distance r_p and injection time of the clouds in RunA (top panel) and RunB (bottom panel). Each individual cloud is represented as a black dot (numbered in ascending order). The small panels to the right show the r_p cumulative distribution of the injected clouds.

units. Each cloud is injected at a distance $d = 15$ and needs the specification of a time of injection, impact parameter and direction of the orbit.

We construct two series of 30 events, drawing the time between each event from a cumulative Gamma distribution with $k = 2$ and $\theta = 2.5P_0$. We made several draws from the Gamma distribution and picked two markedly distinct sets. In the first set, hereinafter RunA, we perform an ‘aggressive’ feed to the MBHB, with an average $\Delta t \approx 3P_0$ between events. On the other hand, in the second set, hereinafter RunB, clouds are fed to the MBHB with an average $\Delta t \approx 6P_0$, allowing the system more time to relax in between each infalling cloud. Note that when scaled to our fiducial system, the above infall rates correspond to $0.4M_\odot\text{yr}^{-1}$ and $0.2M_\odot\text{yr}^{-1}$ entering the inner parsec respectively, comparable to what is typically found in high resolution simulations of gas-rich high redshift galaxies (see, e.g. [Prieto et al. 2017](#)), and is in broad agreement with observations of post-merger galaxies (see e.g. [Sanders & Mirabel 1996](#); [Naab & Burkert 2001](#)).

Cloud impact parameters are drawn so that the periastris passage is uniformly distributed in the range $r_p \in [0, 2a_0]$, if the MBHB was replaced by a single MBH sitting at the origin of the coordinate system and the potential well was ignored. A uniform periastris distribution corresponds to a standard impact parameter distribution $p(b) \propto b$ at infinity, when the trajectory is dominated by gravitational focusing of the central object, as it is the case in

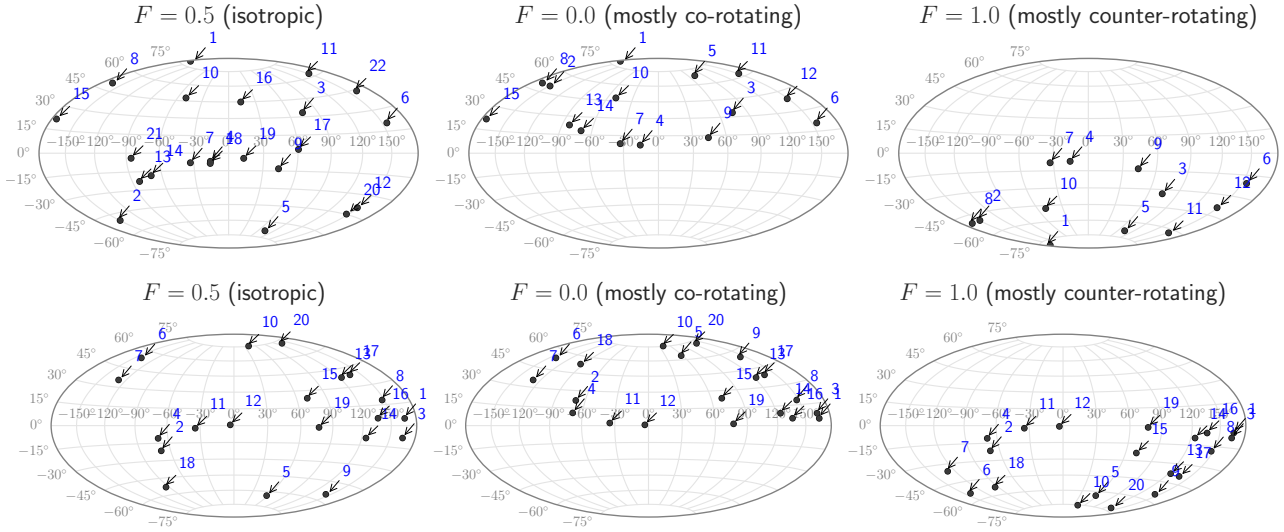


Figure 3. Orientation of the angular momentum of each cloud on the sphere for the three F distributions. In this representation \vec{L}_{bin} points to the north pole. Each panel reports only the clouds that were integrated in that specific run, numbered by injection order. The top row is for RunA and the bottom row for RunB.

Cloud	RunA		RunB	
	$t_i[P_0]$	$\Delta t_i[P_0]$	$t_i[P_0]$	$\Delta t_i[P_0]$
1	0.0	1.87	0.00	3.33
2	1.88	2.22	3.33	8.48
3	4.10	2.46	11.81	6.93
4	6.57	3.61	18.74	8.20
5	10.18	1.60	26.94	10.53
6	11.78	4.32	37.47	6.74
7	16.11	3.42	44.21	4.31
8	19.54	2.53	48.52	4.03
9	22.08	2.47	52.55	2.38
10	24.55	8.85	54.94	13.28
11	33.41	1.29	68.21	5.33
12	34.71	6.86	73.54	4.52
F1p0 13	41.57	7.70	78.06	4.98
14	49.27	2.16	83.04	2.78
15	51.44	1.84	85.82	3.75
F0p0 16	53.28	1.10	89.57	9.16
17	54.39	5.71	98.73	5.63
18	60.10	1.25	104.36	6.20
19	61.36	1.63	110.55	5.53
20	62.99	3.01	116.09	3.12
21	66.01	5.94	—	—
22	71.95	3.49	—	—

Table 1. Cloud injection times in RunA and RunB. For each cloud we report the time of injection (second and fourth columns) and the time to the next cloud injection (third and fifth columns). The two horizontal lines in column 2 and 3 identify the last cloud injection for RunA $F = 1.0$ (after cloud 12) and RunA $F = 0.0$ (after cloud 15), while RunA $F = 0.5$ reached cloud 22. Conversely all RunB configurations reached cloud 20.

our simulations. The injection time and r_p value of each cloud for both RunA and RunB are shown in Figure 2.

After specifying the time of injection and impact parameter, we define the orbit of the incoming cloud by assigning a direction to its orbital angular momentum, \vec{L}_c , with respect to \vec{L}_{bin} . We explore three different sets of initial conditions, defined by the fraction F

of counter-rotating clouds interacting with the MBHB (Dotti et al. 2013):

(i) $F = 0.5$: \vec{L}_c are randomly distributed on the sphere. In this case, on average, 50% of the clouds will be co-rotating and 50% will be counter-rotating with respect to the MBHB. This is known as ‘chaotic’ accretion scenario and is visualised in the left panels of Figure 3.

(ii) $F = 0.0$: all clouds are co-rotating with the MBHB, i.e. they all have $L_{c,z}$ aligned to \vec{L}_{bin} , as shown in the central panels of Figure 3.

(iii) $F = 1.0$: all clouds are counter-rotating with the MBHB, i.e. they all have $L_{c,z}$ counter-aligned to \vec{L}_{bin} , as shown in the right panels of Figure 3.

We first generate 30 random clouds ($F = 0.5$ case) and obtain the $F = 0.0$ and $F = 1.0$ cases by simply ‘mirroring’ \vec{L}_c with respect to the equatorial plane, as shown in Figure 3. The mirroring procedure is crucial to single out the effect of co- and counter-rotation both on the formation of gaseous structures and on the evolution of the binary, because it allows us to consider systems that, besides the flipping of \vec{L}_c , are otherwise identical. Note that once \vec{L}_c and r_p are specified, one still has the freedom to rotate the orbit of the cloud within its orbital plane. To define the orientation of the cloud orbit, we consider the intersection of its orbital plane with the x, y plane defined by our coordinate system, and we place r_p at an angle Θ randomly drawn in the range $[0, 2\pi]$. All the mathematical details of the generation of the initial conditions are given in Appendix A.

Although we generate 30 clouds for each set of initial conditions, we only show initial conditions for 22 clouds for RunA, and 20 clouds for RunB in Figure 2 and 3. Due to time constraints and necessary maintenance of the computer clusters employed for the calculation, we were in fact only able to integrate RunA $F = 0.0$ up to cloud 15, RunA $F = 0.5$ up to cloud 22 and RunA $F = 1.0$ up to cloud 12. All RunB were integrated up to cloud 20. The full information about the initial condition of each cloud, including initial positions and velocities, are given in Appendix A.

In summary, we generated two sets of runs, RunA and RunB defined by different cloud impact parameters and injection times. For each of the runs we considered three angular momenta distributions, $F = 0.0$, $F = 0.5$ and $F = 1.0$, for a total of six different sets of initial conditions. Each of the sets is integrated at four single cloud resolutions: 50k, 200k, 500k and 1m. In the following, we will concentrate on the results of the 50k simulations, which reached the larger number of clouds in the system. Runs at higher resolutions are obviously slower; for example, only 4-5 clouds are generally injected in the 1m case. Higher resolution runs are used as benchmark for comparison and to assess convergence of the simulations.

To study the relaxation of the system after the infall of several clouds, we also ‘forked’ each of the 50k runs after the injection of 5 and 10 clouds. In practice, we ran in parallel two additional sets of simulations in which the system was allowed to evolve unperturbed after 5 and 10 clouds interacted with the binary, to study the long term properties of the relaxed system.

Commonly for this type of numerical investigations, a large computational infrastructure was needed to handle the required set of runs and tests.

4 RESOLUTION AND CONVERGENCE TESTS

The simulations presented in this work feature complex dynamics of multiple clouds interacting with a MBHB, it is therefore important to test the incidence of our main numerical assumptions on the evolution of the system, to keep the impact of spurious numerics under control. The tree reconstruction frequency has been tuned to optimise angular momentum conservation, as described in Section 2.2.1, and softening has been chosen to guarantee a proper resolution of the gravitational interaction between particles. The other numerical ‘degrees of freedom’ are the choice of r_{sink} and of the number of particles used to simulate each cloud, N_c (i.e. the ‘resolution of the simulation’). In this section we check the robustness of our set-up against our choice of these parameters.

4.1 r_{sink} value and accretion convergence

Ideally, a particle will be accreted when it approaches the MBH at about $r = 6GM/c^2 = 3R_S$, where R_S is the Schwarzschild radius. If we consider our fiducial system, this distance is $\approx 5 \times 10^{11}$ cm, equivalent to 2×10^{-6} in code units. It is clear that a realistic condition for particle accretion is beyond any feasible resolution in our numerical scheme. Thus a fictitious sink radius is introduced by hand, as explained in Section 2.2.1. The numerical value of r_{sink} is set *ad-hoc* for numerical convenience. To test its impact on the dynamics of the system we ran four otherwise identical simulations with $r_{\text{sink}} = 0.1$ (standard model), 0.05, 0.2 and 0.5 in code units thus spanning an order of magnitude. For these test simulations we considered RunA $F = 0.0$, with 200k resolution.

Figure 4 shows the evolution of the key parameters describing the evolution of the MBHB in the four runs, evolved for about 25 initial binary orbital periods, sufficient to follow the strong dynamical interaction with eight subsequent clouds. Results match so well across the runs that we had to offset the lines, otherwise they would overlap almost perfectly. The value of r_{sink} does not appreciably impact any of the MBHB parameters, not even the eccentricity evolution, which depends on a fine balance between energy and angular momentum exchanges, and

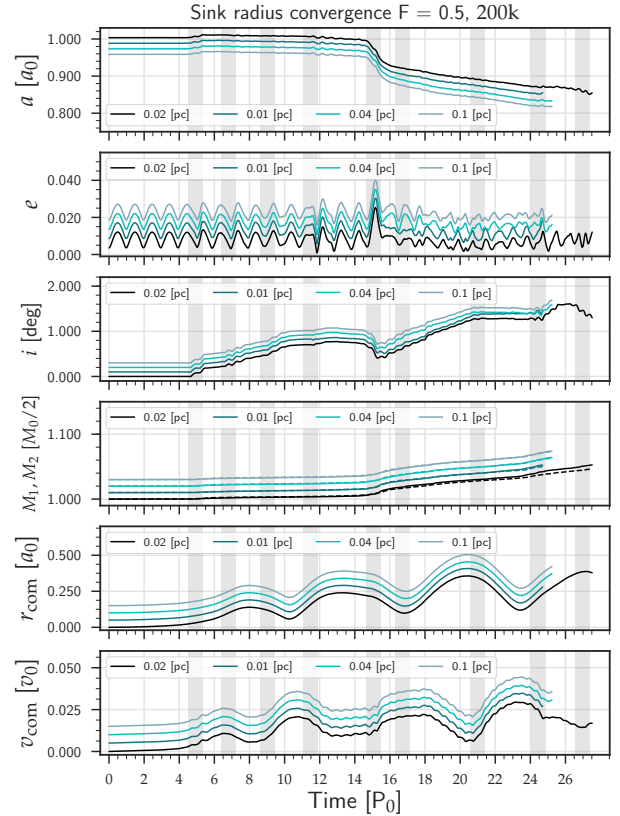


Figure 4. Time evolution of the relevant MBHB parameters in RunA $F = 0.0$, with 200k, for different values of r_{sink} , displayed in simulation units. In each plot, the black line is for $r_{\text{sink}} = 0.1a_0$ (the adopted default values), while different shades of blue are for $r_{\text{sink}} = 0.05a_0, 0.2a_0, 0.5a_0$. Note that lines have been progressively shifted upwards for clarity, since they would otherwise almost perfectly overlap. Grey vertical stripes indicate the ‘arrival time’ of each new cloud, i.e. the time of first periastron passage in its orbit around the MBHB. In the mass panel (fourth from the top), solid and dashed lines represent M_1 and M_2 respectively, normalised to their respective initial values.

is therefore sensitive to minor fluctuations in the dynamics. Note that the pool of interacting clouds span a large dynamical range, including clouds with $r_p < a_0$ (clouds 5 and 8, see figure 3) whose dynamics might in principle be severely affected by an improper treatment of r_{sink} .

Critically, the evolution of the two MBH masses is independent on r_{sink} , which indicates that gas accretion is not affected by its unphysically large value. This is because of the conditions spelled in §2.2.1, whereby particles are required to be *bound* to the MBH for being accreted. In practice only particles that settle into orbits enclosed in the MBH Roche Lobe can be accreted. These particles form eccentric (either transient or persistent) mini-disks that are continuously perturbed by infalling material and are swiftly drained into the sink. Therefore, setting a smaller sink radius only causes a small delay in the time at which a particle is recorded as accreted. Note that this does not mean that all particles crossing r_{sink} will be accreted in reality, as we will discuss in the next section.

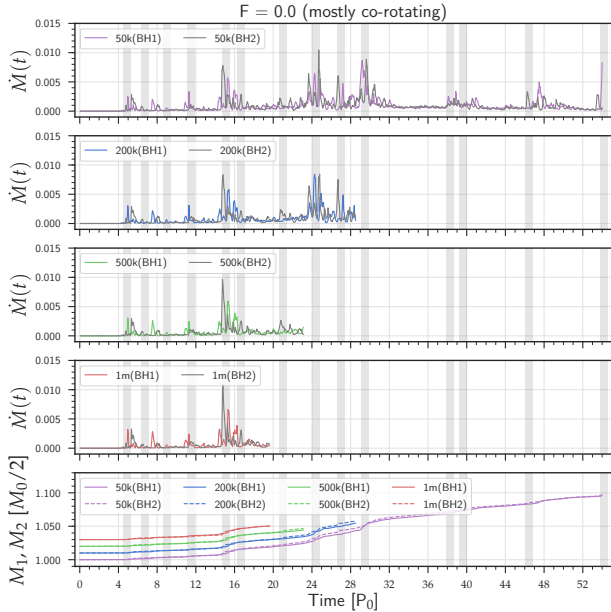


Figure 5. Accretion rate for RunA $F = 0.0$ for all the investigated resolutions: 50k, 200k, 500k and 1m, from top to bottom. The two lines on each panel represent accretion onto each MBH. Orange vertical lines mark the moment each cloud is injected into the system, and grey vertical stripes the time of the first close interaction with the MBHB. Rates are displayed in simulation units $[M_0/P_0]$. The bottom panel shows the mass evolution of each MBH at all resolutions. Lines have been progressively shifted upwards for clarity.

4.2 Robustness against N_c

It is obvious that the level of dynamical detail that traceable in a numerical simulation critically depends on its resolution, and the SPH technique is no exception to this rule. Simulations shall be performed with a number of particles sufficient to resolve the physical features of interest in an N -independent fashion. Of particular interest for this work are accretion onto the MBHB and the distribution of non accreted gas around the binary. To test that our simulations are ‘well behaved’ we ran each of them at the four particle resolutions 50k, 200k, 500k and 1m particles, thus spanning a range of 20.

In Figure 5, we show the accretion rate on each individual MBH in the case RunA $F = 0.0$, for all values of N_c . Accretion is highly variable, showing prominent intermittent spikes in correspondence to the arrival times of clouds with small impact parameters. Note that, at peak, $dM/dt > 0.005P_0^{-1}$ on each individual MBH. Converted to our fiducial system this is about $0.6M_\odot\text{yr}^{-1} \approx 60\dot{M}_{\text{Edd}}$. The actual fate of the gas during these high accretion episodes is unclear. Photon trapping might allow gas to be accreted at super-Eddington rates (e.g. Abramowicz et al. 1988; Ohsuga et al. 2005), or alternatively, radiation pressure might cause the expulsion of the majority of the gas in powerful winds, as observed in (e.g. Tombesi et al. 2010, 2015). As discussed in Goicovic et al. (2017), the fate of the gas in itself has only a minor impact on the dynamical evolution of the system, which is driven more by gas capture from the MBHB, rather than gas accretion. Winds can, however, strongly interact with the surrounding infalling clouds, affecting their dynamics. We caution that this effect is not captured in our simulations. Nevertheless,

Figure 5 shows that, despite minor differences in the definition of the accretion peaks, neither the accretion rate nor the total mass growth of the MBHs have an appreciable dependence on the amount of particles used in the simulation.

To test the dependence of the gas distribution on N_c , we show in Figure 6 the angle-averaged gas density as a function of radius for all RunA at $T = 10.2P_0$, after the disruption of the third cloud. The density is displayed in physical units, by scaling the results to our fiducial system ($M_{\text{bin}} = 10^6 M_\odot$). Density profiles are equivalent at all resolutions, even though they are noisier in the 50k and 200k runs, due to the smaller N_c . Increasing the number of particles allows to better capture fine details in the gas distribution. For example in the $F = 0.0$ case (left panel), the sharp density drop around 0.15pc is better resolved in the 1m run. Likewise, in the $F = 1.0$ case (right panel) the larger amount of particles in run 500k and 1m allows the resolution of two density peaks around 2.2pc, which are blended into a single peak in runs 50k and 200k. Nevertheless, differences are minor, and the overall structure of the gas distribution is preserved across resolutions.

A visualisation of the 3-D particle distribution is shown in Figure 7, where snapshots of the $F = 1.0$ case at $T = 10.2P_0$ are shown in the $x - y$ and $x - z$ plane. The overall gas distribution is exquisitely consistent at all resolutions, even though structures appear slightly blurrier going from the right to the left. The aforementioned difference in the density peaks at 2.2pc, is due to the regions highlighted with black circles on the rightmost column. Looking at this critical areas, and moving left in the panel sequence (going down in resolution), the dense areas become less defined eventually blending the fine structures in larger clumps. These differences, however, do not affect the overall dynamical evolution of the systems and are relevant only in the determination of the statistics of dense clumps prone to star formation. Since this specific investigation is beyond the scope of the current work, we deem the 50k runs sufficiently accurate for our purposes.

5 RESULTS

In this section we present the main results of the simulations concerning the formation and evolution of gaseous structures around the MBHB⁴. In a companion paper (Goicovic et al. (2018)) we focus on the evolution of the MBHB. We will describe the general outcome of both RunA and RunB, in order to make comparisons between the two. When a specific aspect is investigated in more depth, we consider RunA as default case. We also ran an extra suite of simulations, that we call RunC, mixing the cloud configuration of RunA and the time distribution of RunB. Some relevant results for this extra suite of runs is presented in Appendix B. In the figures of this Section, relevant quantities are displayed in physical units, scaled to our fiducial system (i.e. a MBHB with initial mass $M_{\text{bin}} = 10^6 M_\odot$ and initial separation $a = 0.2\text{pc}$), whereas run snapshots are shown in simulation units ($M_{\text{bin}} = a = 1$).

5.1 Overall evolution of the gas distribution

We first look at the evolution of the (angle averaged) gas density profile as a function of distance to the MBHB centre of mass. This

⁴ Animations of all the simulations can be seen in <http://multipleclouds.xyz/movies/>

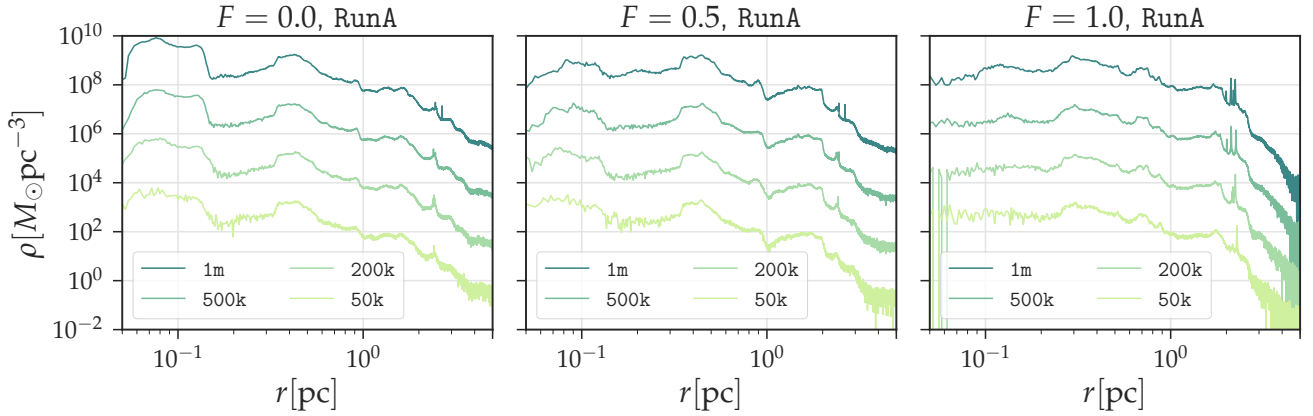


Figure 6. Angle-averaged density profile at $T = 10.2[P_0]$. In each panel, from bottom to top, lines corresponds to resolution 50k, 200k, 500k and 1m, and have been shifted upwards to ease comparison. The three different F -distributions are represented from left to right, as indicated in figure. The y -axis normalisation of the 50k resolution is fixed to the scale of our fiducial system, $M_{\text{bin}} = 10^6 M_\odot$.

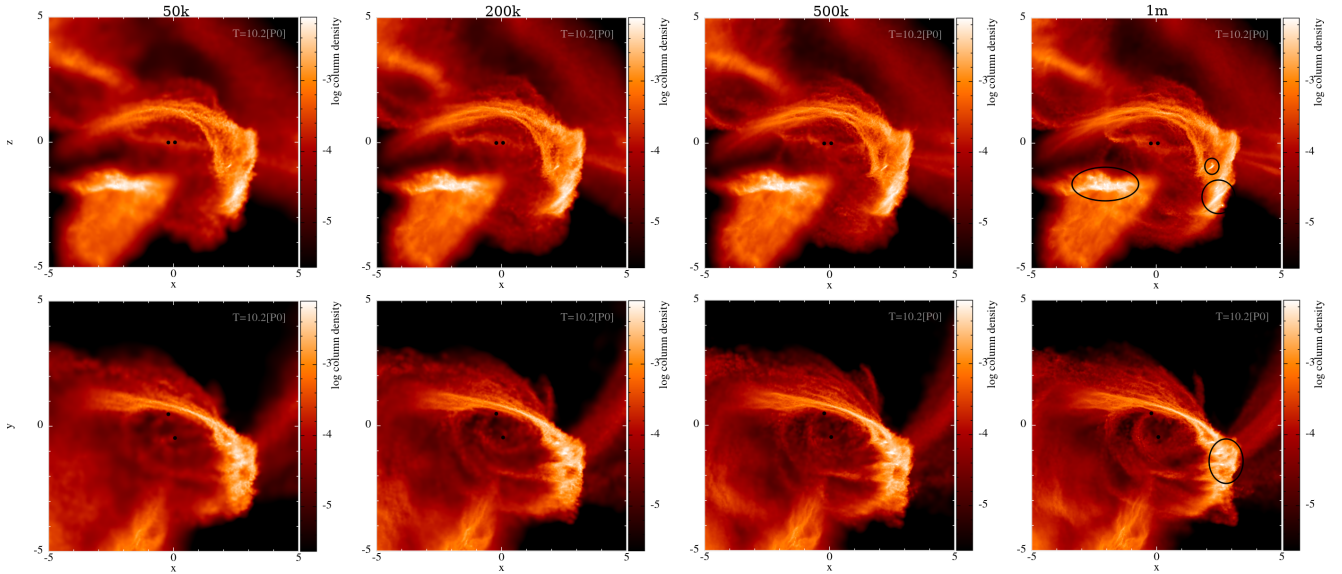


Figure 7. Column density rendering of RunA, $F = 1.0$ at $T = 10.2[P_0]$. Each column represents a cloud resolution, 50k, 200k, 500k and 1m from left to right. In each column, the top and the bottom panels represent views in the $x-z$ and $x-y$ plane respectively.

is shown Figure 8 as runs advance and more clouds are added to the system. As a general trend, we see that in all cases the gas density outside the binary orbit tends to follow a $\rho \propto r^{-2}$ distribution, even though the profile is necessarily time dependent and there is a large scatter. In the long run, this has to be expected; by throwing gas at the binary from all directions, the resulting envelope will be almost at rest with respect to the binary centre of mass. One can then estimate the Bondi radius as $R_B = 2GM/c_s^2$. For our fiducial system, the gas temperature is $T = 100$ K, resulting in $c_s \approx 2 \text{ km s}^{-1}$. This means that the Bondi radius is several tens of parsecs i.e. much bigger than the domain of the simulation. We are hence injecting within the Bondi radius of the binary gas at a roughly constant rate, which is therefore expected to settle into an r^{-2} density profile.

The “humps” – observed for example in the middle top-panel

on the 22th cloud line around 5pc, or bottom-right panel at 0.5pc and 1pc for the 10th and 15th cloud lines, respectively – correspond to new clouds infalling into the system, and are not properties generated by bound material that is falling back to the binary after cloud disruption. Each new infalling cloud will generate a “hump” that will move from right to left until is disrupted by the MBHB. Conversely, the sharp lines accumulating at $R > 1\text{pc}$ are due to high density clumps formed during the phase of cloud compression in the interaction with the MBHB and then ejected at large distances.

The figure also highlights few interesting features specific to each of the F -distributions. On the $F = 0.0$ panels (left column) we can observe a clear dip in the density profile around 0.2-0.3pc, comparable to the binary orbital separation, building up over time as more clouds get into the system. This is a clear

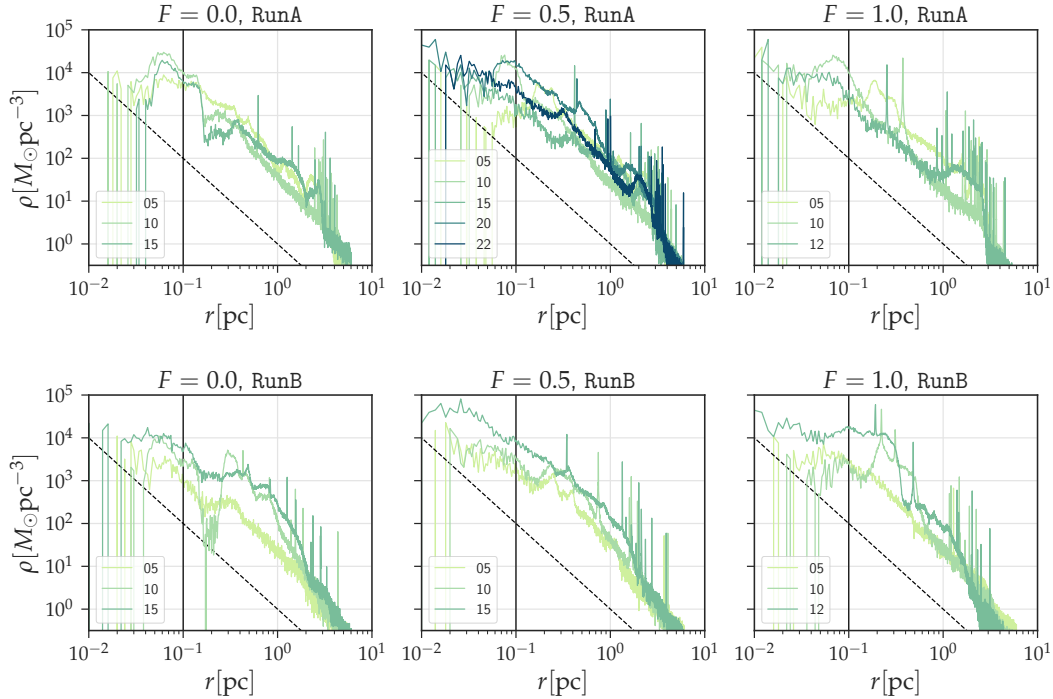


Figure 8. Angle-averaged mass density profile for all 50k runs (as indicated in each panel) at different snapshots, in physical units, scaled to our fiducial system. Curves are labelled by the number of clouds present in the system, and represent the density profile at the last recorded snapshot before the subsequent cloud is injected in the system (e.g.: 05 represents the status of the system at the last snapshot before adding the 6th cloud). In each panel, the dashed line refers to a $\rho \propto r^{-2}$ profile, for comparison. The solid vertical black line shows the initial position of each of the MBHB components.

indication that the action of the MBHB is carving a cavity in the gas distribution. In fact in the $F = 0.0$ case, clouds are mostly co-rotating and we expect a lot of gas will re-arrange in a co-rotating circumbinary structure. Lindblad resonances are then expected to carve a hole in the gas distribution of a size of $\approx 2a$ (Artymowicz & Lubow 1994). The large overdensities at the MBH location are instead indicative of prominent mini-discs, that are also expected to form in the co-rotating case (Goicovic et al. 2016). Note, moreover, how the density just outside the cavity in RunB builds up with time much more prominently than in RunA, which is a sign that a more massive circumbinary disc is being built in the former case (as we will see below, cf Figure 9 and Figure 11). Conversely, clouds are mostly counter-rotating in the $F = 1.0$ case (right panels), and Lindblad resonances do not operate. No steady dip is in fact observed in this case, however prominent transient overdensities can be seen forming around 0.2pc, which are indicative of the formation of compact dense rings that get disrupted in the interaction with new incoming clouds (again, see example in Figure 11). The isotropic nature of the $F = 0.5$ runs can be also appreciated (central panels), which shows a relatively smooth and steady shape. In the following, we will examine in detail the evolution of these gas structures, paying particular attention to the formation of mini-discs, circumbinary discs and rings.

5.2 Circumbinary structures

Following the infall of each cloud, some of the non-accreted material will remain bound to the binary, forming structures around it, as well as around each MBH. Previous work by Goicovic et al. (2016) studied the impact of the orbital configuration of the

infalling cloud on the formation of such structures, showing a rich phenomenology depending on the initial orbital inclination relative to the MBHB plane and impact parameter. In particular they found that the binary is generally unable to change significantly the orientation of the gas, which produces discs that follow the initial cloud's inclination.

For the simulations presented in this paper, the incoherence of the accretion events produces a variety of gaseous streams that continue interacting with the binary and between each other, making a clear identification of circumbinary disc structures much harder. To study any type of stable structure around the MBHB is essential to devise a set of conditions defining whether an SPH particle belongs or not to that structure. In practice we define circumbinary structures by considering all particles that:

- are bound to the MBHB (to avoid including unbound streams of gas flung away in the interaction with the MBHB);
- are inside a critical radius $r < 7a_0$. The specific choice is arbitrary, but is motivated by the typical size of circumbinary discs found in Goicovic et al. (2016).

For each SPH particles identified by this first cut, we can take 3-D position and velocity, replace the MBHB with a point mass centred in the centre of mass of the system, and compute a Keplerian orbit around this point. This calculation is an approximation of the true orbit of the particle, since it ignores the binary nature of the central massive object, as well as the external potential. The advantage of this approach is that it allows to define orbital elements such as semimajor axis a , eccentricity e and inclination i for each particle. We therefore impose the further condition that the particle orbit

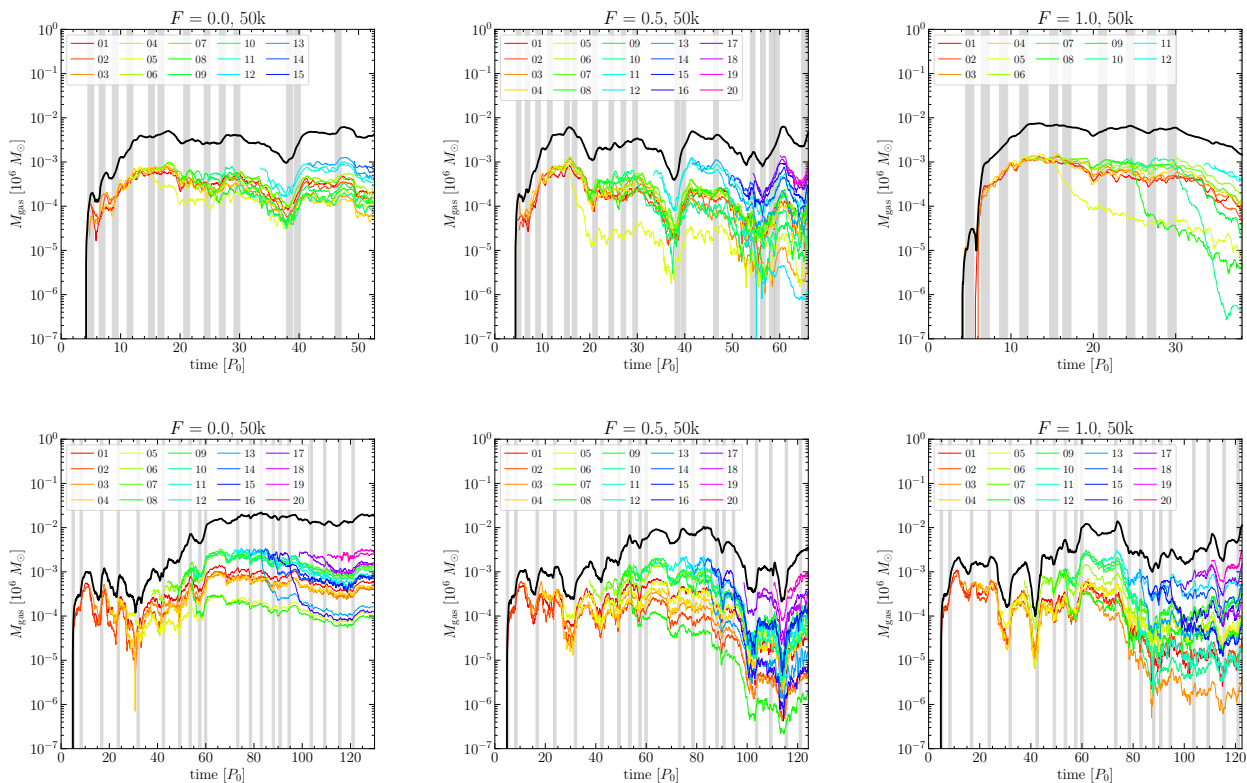


Figure 9. Mass evolution of the circumbinary structure for the models $F = 0.0$ (left), $F = 0.5$ (centre) and $F = 1.0$ (right). The first row represents RunA while the bottom row represents RunB. The different coloured lines are the mass contribution from each infalling cloud while the black line is the sum of the contribution from all clouds

- has $a(1 - e) > 1$, to make sure that it does not intersect the MBHB;
- has $e < 0.9$. Although this is also a somewhat arbitrary choice, it allows to exclude particles belonging to new infalling clouds (which are on almost radial orbits).

Figure 9 shows amount of gas that meets the aforementioned conditions as a function of time, together with the breakdown of the contribution of each individual cloud. Despite stochasticity and differences between the runs, we identify some general trends. As new clouds get into the system, their contribution to the circumbinary structure initially rumps up to $M \approx 10^{-3} M_{\text{bin}}$ (i.e. 10% of the initial mass cloud), since material settles on orbits with $a < 7a_0$ and circularises to $e < 0.9$. This process is evident for the initial clouds in RunA which have fairly large periapsis passage and tend to not interact with each other (cf the top panel of Figure 2). Up to $T \approx 15P_0$, the circumbinary structure mass tends to steadily grow in time to about 1% of the MBHB mass. Eventually, incoming new clouds on intersecting orbits prompts accretion of pre-existing circumbinary gas, preventing the structure to significantly further grow in mass. This is why the total mass in these structures never grows to much more than few% of the MBHB mass. This process is more evident right from the start in RunB. In this case, the first clouds have rather small periapsis and they strongly interact with each other upon arrival onto the MBHB. The net effect is that the circumbinary structure does not grow much beyond $M \approx 10^{-3} M_{\text{bin}}$ until a number of clouds with larger periapsis contribute a substantial mass budget from $T \approx 40P_0$ onwards (cf the bottom panel of Figure 2).

It is clear that the contribution of each individual cloud to the circumbinary structure tend to decrease in time (although with large fluctuation). With “older” clouds contributing less to the mass budget. This causes the large rainbow-like spread towards the end of the runs, whereby the contribution of each individual cloud ranges between 10% to about 0.01% of their initial mass. It is interesting to note that the spread is much larger in the $F = 0.5$ and $F = 1.0$ cases, in which clouds experience more violent interactions among themselves and with the binary. In the $F = 0.0$, conversely, most of the circumbinary material is stored into a disc held-up by Lindblad resonances. The income of new clouds in mostly co-rotating orbit tends to add new material to the disc without a substantial disruption of the pre-existing conditions. For example, the first incoming cloud (red curve) still contributes about 5% of its mass to the circumbinary disc by the end of the simulations in both RunA and RunB.

Although Figure 9 quantifies the amount of material that forms a circumbinary structure, it does not provide much information about the nature of that structure. For example, the gas might be configured in a disc or in a cloud or in multiple rings and it would not make a difference. For each SPH particle belonging to the structure, we reconstructed the orbit and we computed a , e and i . We can now construct the distributions of these quantities, and follow their evolution in time.

This is shown in Figure 10 for all our runs, together with a replication of the total circumbinary gas mass shown in figure 9 (top rows). Each panel is built as follows. We take a uniform grid in the desired quantity and, at each simulation snapshot, we construct an histogram by adding particles to the bins and

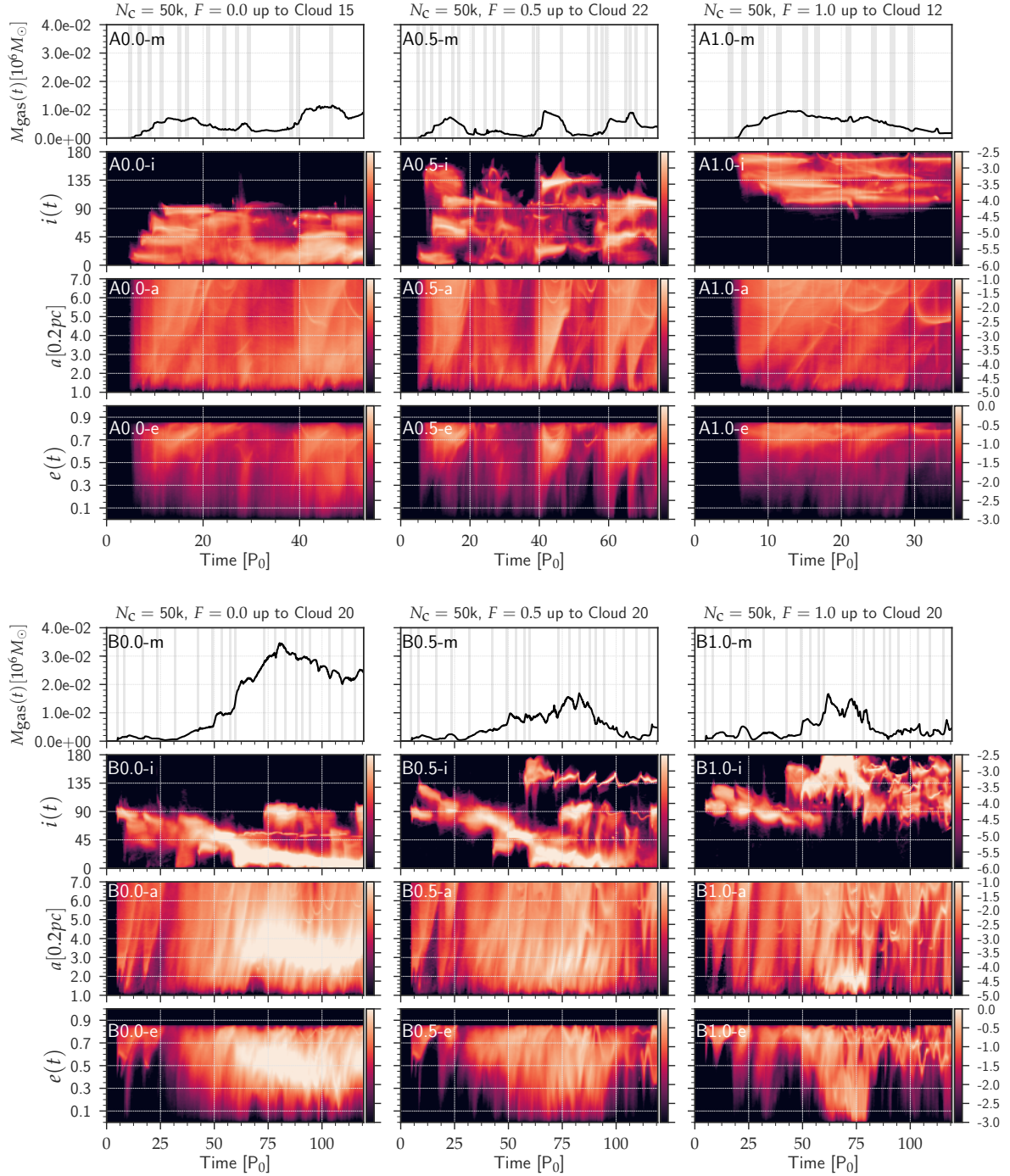


Figure 10. Time evolution of the circumbinary structure in each of the simulations. The three columns, left to right, are for the $F = 0.0$, $F = 0.5$ and $F = 1.0$ scenarios; the top 3×4 grid of plots is for RunA and the bottom for RunB. In each grid, the top row shows the time evolution of the total mass of the structure, M_{gas} . All the other rows show in log-scale the time evolution of selected particle distributions, normalised so that the integral of any vertical slice of any panel gives the total mass M_{gas} at that specific time. With such normalisation, the second row represents dM_{gas}/di , the third row dM_{gas}/da (a is displayed in units of initial binary separation) and the forth row dM_{gas}/de . The colour gradient is displayed in log-scale, as indicated by the bars at the far right of each row. Grey lines on the M_{gas} panels, indicate the time of arrival of infalling clouds.

normalising so that the integral over the bins gives the total mass in the structure. Histograms at subsequent steps are then concatenated along the x -axis and smoothed to produce the 2-D density maps displayed in the figure (in logarithmic scale). Figure 10 clearly show the connection between the F -distribution and the geometry

of the circumbinary structures for both RunA and RunB. We now describe the diverse phenomenology of each F -distribution, referring to representative examples of each individual case shown in Figure 11.

For the co-rotating case ($F = 0.0$, left column), after an

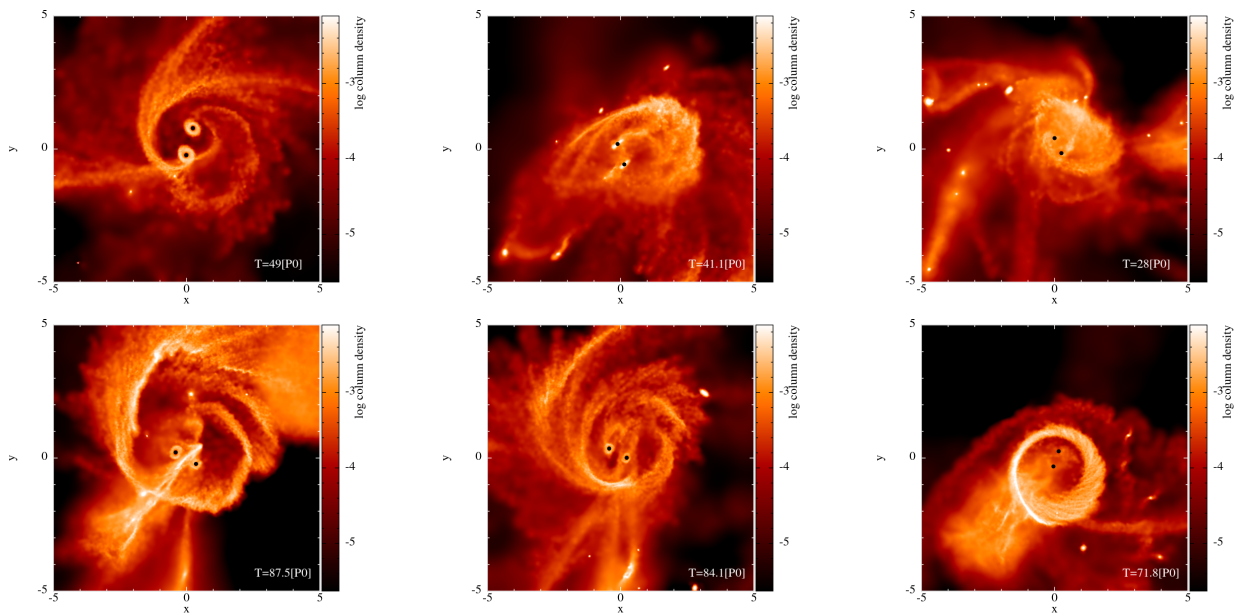


Figure 11. Snapshots of RunA (top row) and RunB (bottom row) at selected time (as indicated in each panel), highlighting features described in figure 10). In all panels, the binary is viewed face-on in the $x - y$ plane, and the gas column density (integrated along the z -axis) is shown in log-scale as indicated on the right of each panel.

initial transient phase, most of the particles have less than 50° respect to the binary, and tend to distribute in a co-rotating, extended circumbinary disc, displaying a variety of eccentricities. In RunA, the disc does not build up as a coherent structure, as hinted by the low total mass (panel A0.0-m) and large range of inclinations (panel A0.0-i). The presence of large amount of gas at high inclinations, prevents resonances from being efficient, and a well defined cavity cannot be seen in panel A0.0-a, where we see gas been distributed in the whole range $1 < a < 7$, although a concentration of gas at $a < 5$ appears from $T \approx 40P_0$ onwards. Conversely, in RunB, a prominent thin disc builds up coherently and progressively aligns with the MBHB. This is demonstrated by the mass build-up up to about $M_{\text{gas}} = 0.03M$ (panel B0.0-m) and by the narrow range of inclinations decreasing with time (panel B0.0-i). The density contrast in panel B0.0-a highlights that the bulk of the disc lies in the range $2 < a < 4$, with the decline at $a < 2$ indicative of the resonance-sustained cavity. Gas within the disc remains in fairly eccentric orbits spread around $e = 0.5$ (panel B0.0-e).

The left column of Figure 11 displays representative snapshots of these two simulations. The top panel is taken when the 13th cloud of RunA $F = 0.0$ interacts with the system, at $T \approx 49P_0$. An extended circumbinary structure, almost in the binary orbital plane ($i \approx 20^\circ$) is clearly visible, but it is about to be partially disrupted by the 13th cloud streaming-in from the left (which will cause the subsequent drop in M_{gas} observed in panel A0.0-m). The bottom panel shows the status of RunB $F = 0.0$ at the peak of M_{gas} at $T \approx 95P_0$. Comparisons between the two highlights the prominence of the circumbinary disc forming in RunB, featuring a massive spiral that extends to $a \approx 5$,

Not surprisingly, in the counter-rotating case ($F = 1.0$, right column), the gas distribution around the binary has high inclinations. Also in this case, the two runs display quite different behaviours. In RunA, we see the formation of a persistent structure. The mass gets to $M_{\text{gas}} \approx 10^{-2}M$ at the peak, declining to

$M_{\text{gas}} \approx 10^{-3}M$ by the end of the simulation (panel A1.0-m), is spread across the whole a range (panel A1.0-a), and displays a wide range of inclinations (panel A1.0-i). The gas essentially configures into a tenuous and low mass counter-rotating cloud. This is clearly shown in the top right panel of Figure 11 taken at $T = 28P_0$; no clear disc-like structure is present, and the binary is surrounded by a relatively compact cloudy envelope with streams extending to $a > 5$.

The situation is strikingly different in RunB. Here we see that the violent interaction with the binary causes most of the gas to be either accreted or expelled and no steady circumbinary structure is formed. A prominent eccentric transient ring forms around $T = 60P_0$, being disrupted about 20 periods later (note that in our fiducial system the ring would last for about 0.2 Myr), as clear from panel B1.0-m. The structure is almost perfectly counter-aligned to the binary (panel B1.0-i), is confined within $a < 2.5$ (panel B1.0-a) and has an average eccentricity $e \approx 0.3$ (panel B1.0-e). The ring is clearly visualised in the bottom right panel of Figure 11.

The $F = 0.5$ simulations, shown in the central column of Figure 10, highlight the impact of the specific cloud distribution on the formation of circumbinary structures. RunA features a number of transient, incoherent structures extending at all radii (panel A0.5-a) and inclinations (panel A0.5-i). The top central panel of Figure 11 shows the system at $T = 41P_0$. Cloud 12 and 13 are bringing fresh gas into the system, causing a temporary enhancement of the mass in the circumbinary structure, that looks like an incoherent, extended envelope. Conversely, RunB shows a behaviour similar to the $F = 0.0$ case; at $T \approx 60P_0$, a co-rotating circumbinary structure forms, progressively aligning with the MBHB as it gains mass in subsequent interactions (panels B0.5-m and B0.5-i). The structure persists for about 30 binary orbits (≈ 0.3 Myr, when scaled to our fiducial system), before being completely disrupted by the arrival of new clouds on small pericentre orbits (clouds 13-to-16, cf Figure 2). A snapshot of the system at $T = 89P_0$, shown in the bottom central panel of

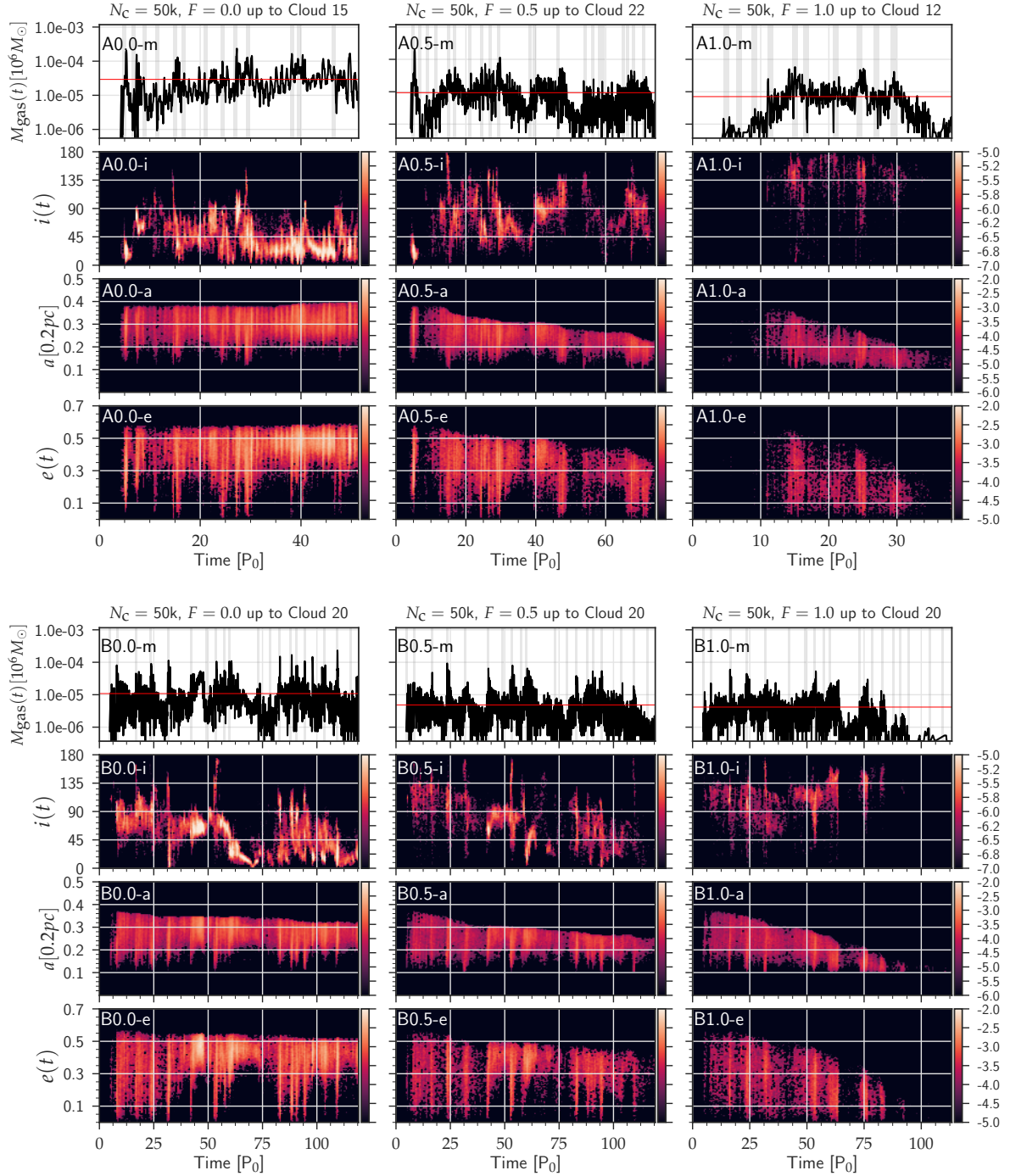


Figure 12. Same as Figure 10 but for the mini-disc of MBH1 in the $F = 0.0$, $F = 0.5$ and $F = 1.0$ cases (left to right), for RunA (top 3×4 grid) and RunB (bottom grid). Each panel is labelled as in Figure 10, note the log-scale in the top rows showing the total mass in the mini-discs, M_{gas} .

Figure 11, highlights the similarity with the $F = 0.0$ run; in this case, the circumbinary spiral is less massive and slightly more compact.

Interestingly, in both RunA and RunB, there is the tendency to form more co-rotating than counter-rotating structures. This can be clearly seen in panels A0.5-i and B0.5-i of Fig. 10, where the particles tend to cluster below 90 degrees in inclination even though half of the events come from the southern hemisphere. This occurs simply because resonances with the MBHB orbital motion

efficiently transfer angular momentum to co-rotating gas, which can therefore settle into more extended and stable structures. An effect that is absent for the counter-rotating material.

5.3 Mini-discs

It is also interesting to study the dynamics of gaseous structures *inside* the MBHB corotation radius, which are generally directly responsible for the binary feeding and the associated high energy

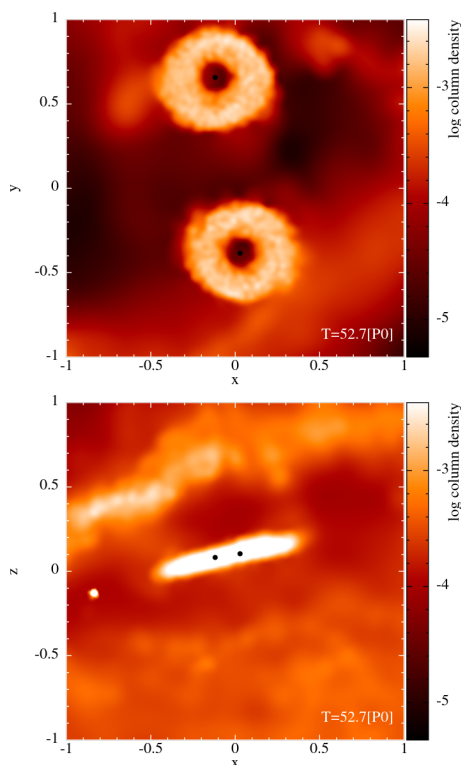


Figure 13. Snapshot of the last stage of RunA $F = 0.0$ (shown in Figure 12, first column of the top grid). The top and bottom panels show the $x - y$ and $x - z$ views respectively.

Simulation	Distribution	$M_{MD1}[10^6 M_\odot]$	$M_{MD2}[10^6 M_\odot]$
RunA	$F = 0.0$	3.58×10^{-5}	3.39×10^{-5}
	$F = 0.5$	6.64×10^{-6}	6.82×10^{-6}
	$F = 1.0$	1.17×10^{-6}	9.93×10^{-7}
RunB	$F = 0.0$	1.08×10^{-5}	1.07×10^{-5}
	$F = 0.5$	4.84×10^{-6}	5.15×10^{-6}
	$F = 1.0$	4.15×10^{-6}	4.32×10^{-6}

Table 2. Average mass of the mini-discs surrounding the MBHs in all our runs.

electromagnetic radiation. In the standard picture of a steady circumbinary disc, the forcing imposed by the binary quadrupolar potential induces gas streams that feed prominent mini-discs around each MBH (D’Orazio et al. 2013b). Conversely, in the counter-rotating case, the absence of Lindblad resonances allows gas at the edge of a putative circumbinary disc to impact directly onto the binary. Since the MBH and the gas have opposite directions, $|\vec{v}_{\text{BH}} - \vec{v}_g| \approx 2v_{\text{BH}}$; this means that the capture cross section of the gas is very small, and only gas *inside* the sink radius becomes bound to the MBH being promptly accreted. In practice, mini-discs extending beyond r_{sink} are unlikely to form in this case.

Similarly to Section 5.2, we now select all particles inside either of the MBH Roche Lobes, defined as circles around each MBH with radius

$$R_{\text{RL}} = \frac{0.49 q^{2/3}}{0.6 q^{2/3} + \log(1 + q^{1/3})} a \quad (8)$$

(Eggleton 1983), where q is the binary mass ratio, which we assume to be unity throughout all of our simulations. We then use 3-D positions and velocities to compute their Keplerian orbit around

the closest MBH. We define the mini-disc around each MBH as the collection of gas particles on orbits that:

- are bound to that MBH;
- have a pericentre larger than the sink radius, i.e.: $a(1 - e) > r_{\text{sink}} = 0.1$ (equivalent to 0.02pc for our fiducial system);
- have an apocentre smaller than the Roche Lobe size, i.e.: $a(1 + e) < R_{\text{RL}}$.

The evolution of the mini-disc around MBH1 in each run is summarised in Figure 12. There we show the time evolution of the mini-disc total mass (top row), and the distribution of inclination (second row), semimajor axis (third row) and eccentricity (bottom row) of the particles belonging to it, constructed as detailed in §5.2. The first thing we notice is that, due to the complex dynamics triggered by the infall of incoherent gas clouds, mini-discs are far from being well defined, stable structures in our simulations. However, some general features of relaxed ‘steady state simulations’ are preserved. In particular, we see that the prominence and persistence of mini-discs is a strong function of F . This is also supported by numbers reported in Table 2, demonstrating that the average mass in the mini-discs is much higher in the $F = 0.0$ runs. Note that this is particularly true for RunA: here the frequent supply of fresh clouds has the effect of feeding the mini-discs in the $F = 0.0$ case, whereas increases the chance of disrupting them quickly in the less coherent $F = 0.5$ or in the counter-rotating $F = 1.0$ cases. In RunB, clouds are supplied at a lower rate, leaving more time for the gas in the mini-discs to be accreted. This mostly affects the $F = 0.0$ run, in which we see a smaller amount of mass accumulating in the mini-discs on average.

In general Figure 12 show that mini-discs are more massive and persistent in the $F = 0.0$ runs (left column). Note that both in RunA and RunB there is a significant scatter in the particle inclination distribution. This is because particles partially preserve memory of the inclination of their parent cloud and tend to form mini-discs aligned with their incoming orbital angular momentum. In the long run, however, the MBHB potential torques the disks causing a partial alignment with its orbital angular momentum (effect visible both in panels A0.0-i and B0.0-i). An example of such persistent mini-discs forming in the co-rotating case is shown in Figure 13, displaying the last snapshot of RunA $F = 0.0$.

As expected, mini-discs becomes much more intermittent as F increases. This is essentially because mini-disc formation is a more natural outcome in the interaction with co-rotating clouds. In fact, we can see that in the $F = 0.5$ case (central column) the formation of structures with $i < 90^\circ$ is strongly preferred (panels A0.5-i and B0.5-i). In the extreme $F = 1.0$ case, mini-discs are very intermittent and, contrary to the circumbinary structures, often show a significant fraction of co-rotating material (i.e. with $i < 90^\circ$, see panel B1.0-i). The shrinking of the binary as the simulations advance, is clearly noticeable in the a and e panels of all the $F = 0.5$ and $F = 1.0$ simulations. In fact, as the two MBHs get closer to each other, their Roche Lobes contract and the size of the mini-discs that they can accommodate shrink accordingly.

Finally, we note that the study of mini-discs is a delicate matter in this kind of simulations, due to the relatively large sink radius and to the inherent small size of these structures which makes their resolution difficult. In fact, even the most prominent mini-discs in the $F = 0.0$ simulations have an average mass of about 10^{-5} , which means that in the 50k simulations they are resolved with about 50 particles. We therefore checked convergence of our results by comparing mini-discs at 50k and 500k resolutions finding

essentially no difference neither in the intermittent behaviour nor in the average masses, indicating that our results are robust. Likewise, we tested that shrinking the sink radius by a factor of two does not appreciably affect the mini-discs evolution.

5.4 ‘Forked’ simulations: stopping the supply of clouds

The variability of a system being constantly affected by multiple chaotic accretion events has clearly emerged in the previous sections, where we showed the continuous formation and disruption of structures as new clouds were added to the system. An interesting question is what happens when the supply of new clouds ceases and the system is allowed to relax. To answer this question, we took two snapshots from all the RunA simulations at the moment when the 5th and the 10th clouds were added to the system and ‘forked’ them, thus starting two parallel series of runs in which no further clouds were added, allowing the system to evolve unperturbed. We show in this section results from simulations forked after the 5th clouds, the outcome of the ones forked after the 10th cloud are qualitatively very similar.

To illustrate the evolution of the system, we perform the same analysis described in §5.2 and build 2-D density plots to study the main properties of the particles forming both the circumbinary disc, and the mini-discs around each MBH. Those are shown in Figures 14 and 15 respectively. We now discuss the main long term features of the $F = 0.0$, $F = 1.0$ and $F = 0.5$ run separately.

In the left column of Figure 14 we can see that in the $F = 0.0$ run, after the infall of the 5th cloud, the remaining material from the other disrupted clouds falls back forming a prominent circumbinary disc around the MBHB (panel 0.0-m). The disc is relatively thin, with an inclination of about 10° with respect to the binary orbital plane (panel 0.0-i), and it most of the mass is concentrated at a distance $2 \leq a \leq 5$ from the binary centre of mass, with a broad range of eccentricities $0.1 < e < 0.7$ (panels 0.0-a and 0.0-e). The left column of Figure 15 allow us to confirm the long term stability of the mini-discs, which is almost aligned with the MBHB orbital plane.

The circumbinary disc in the $F = 1.0$ simulation (right column) displays a very similar behaviour. Disrupted cloud material falling back on orbits with comparable inclinations, interact with each other leading to the formation of a relatively massive circumbinary disc (panel 1.0-m). From panel 1.0-i, we note that, due to the high initial inclination and to the fact that $L_d \ll L_B$, the disc tends to counter-align with the MBHB (King et al. 2005b). By the end of the simulation, an almost perfectly counter-rotating circumbinary disc has formed, with $i \approx 170^\circ$. The circumbinary disc is much better defined than in the $F = 0.0$ case; particles are mostly confined within $a \leq 2.5$ (panel 1.0-a) and have lower eccentricities $e < 0.3$ (panel 1.0-e). The right column of Figure 15 shows that mini-discs are much lighter, intermittent, and tend to be consumed with time. Note the increase in the mini-disc mass around $T = 35P_0$ (panel 1.0-m), in correspondence of the decrease in the circumbinary disc mass. This is due to a stream of gas partially disrupting the circumbinary structure and feeding gas to the central MBHB.

The $F = 0.5$ simulation does not seem to converge towards a specific relaxed state. The very diverse orbits of infalling clouds prevent the stream to efficiently interact, dissipate angular momentum and circularise into any specific circumbinary structure. In fact, the mass in a putative ‘circumbinary disc’ does not grow in time (panel 0.5-m) and streams at different inclinations are clearly recognisable until the end of the simulation (panel 0.5-i). Figure 15

shows that mini-discs are not very prominent, and also tend to be consumed with time.

A summary of the overall structures formed by the end of these ‘forked’ simulations is displayed on Figure 16. The $x - y$ and $x - z$ views highlight the thin circumbinary discs forming in both the $F = 0.0$ and $F = 1.0$ runs, along with the well defined mini-discs in the former case. Conversely, in the $F = 0.5$ case, no coherent structure is recognisable, and at least four distinct streams originating from different clouds are clearly visible. The aftermath of an epoch of incoherent accretion events is therefore strongly dependent on the properties of the infalling clouds. In general, ordered circumbinary structures persist only if the sum of all infalling material has a substantial net angular momentum (either co- or counter-aligned with the MBHB).

6 DISCUSSION AND FUTURE WORK

In this work we have used detailed SPH simulations performed with a modified version of the code GADGET-3 to study the interaction with a circular, equal mass MBHB with a series of infalling clouds in very eccentric orbits. We performed six main runs, considering two distributions of cloud pericentre distances and arrival times (defining RunA and RunB), and three distribution of angular momenta with different degree of anisotropy that we labelled $F = 0.0$ (co-rotating clouds), $F = 0.5$ (isotropically distributed clouds) and $F = 1.0$ (counter-rotating clouds). The goal is to study the dynamics of the MBHB-gas interaction when the binary is supplied with gas in incoherent discrete ‘pockets’, which might be a typical situation in the turbulent environment of high redshift, gas-rich galaxies (e.g. Prieto et al. 2017) and merger remnants (e.g. Perret et al. 2014), relevant to the early build-up of MBHs (see Volonteri 2010, for a review) and to future low frequency gravitational wave observations with LISA (Amaro-Seoane et al. 2017b). The main focus of this paper was on the formation and evolution of bound gaseous structures, in a companion paper (Goicovic et al. 2018) we will turn our attention on the evolution of the MBHB.

Our main findings are summarised in the following points.

Post interaction gas distribution. In general, the density profile distribution of the gas post-interaction with the MBHB follows a $\rho_{\text{gas}} \propto r^{-2}$ distribution. This is expected since the speed of sound of the gas is just few km s^{-1} , implying a large Bondi radius of the MBHB, extending beyond the bulk of the extended gas. Compression of the clouds at pericentre also causes the formation of several, extremely dense self-gravitating clumps that can be favourable sites for *in-situ* star formation. In this work, we stopped gravitational collapse of the clumps by imposing an adiabatic behaviour of gas region above a critical gas density.

Circumbinary structures. Many theoretical and numerical studies of MBHB evolution in gaseous environments rely on the presence of a relatively stable, extended circumbinary disc that can efficiently extract energy and angular momentum from the binary (e.g. MacFadyen & Milosavljević 2008; Cuadra et al. 2009; Roedig et al. 2011; Kocsis et al. 2012b; Tang et al. 2017b). However, the route to the formation of such stable, extended disc has hardly been investigated. Our simulations show that, when the gas is fed to the binary in incoherent pockets, it is hard to form a massive circumbinary structure. Adding more clouds to the system is a two-edged blade: on the one hand, new clouds supply fresh material that can add-up to the mass budget of the disc; on the other hand, clouds intersecting at high inclinations with a pre-existent disc can

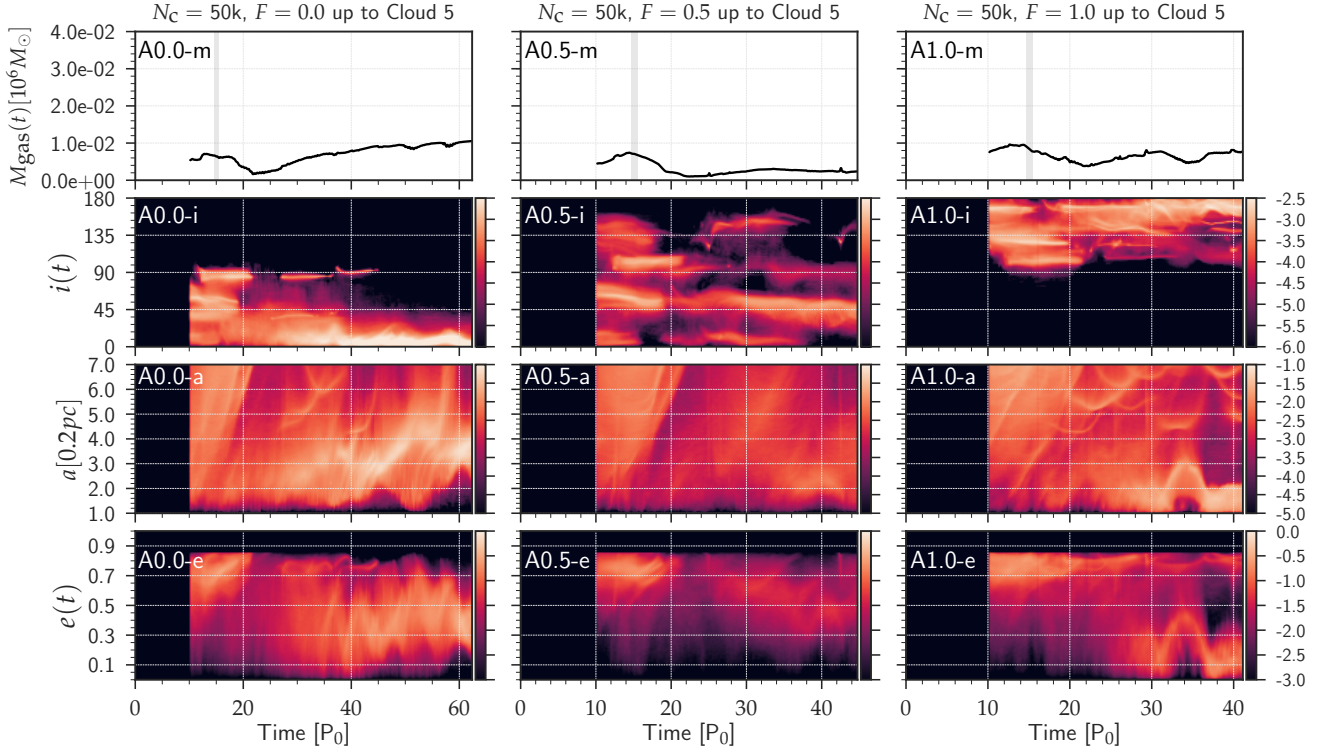


Figure 14. Same as Figure 10 but for the set of ‘forked’ simulations. The $F = 0.0$, $F = 0.5$ and $F = 1.0$ distributions are shown from left to right. The vertical grey stripes in the first row mark the time of arrival of the 5th cloud. No further cloud is included into the system.

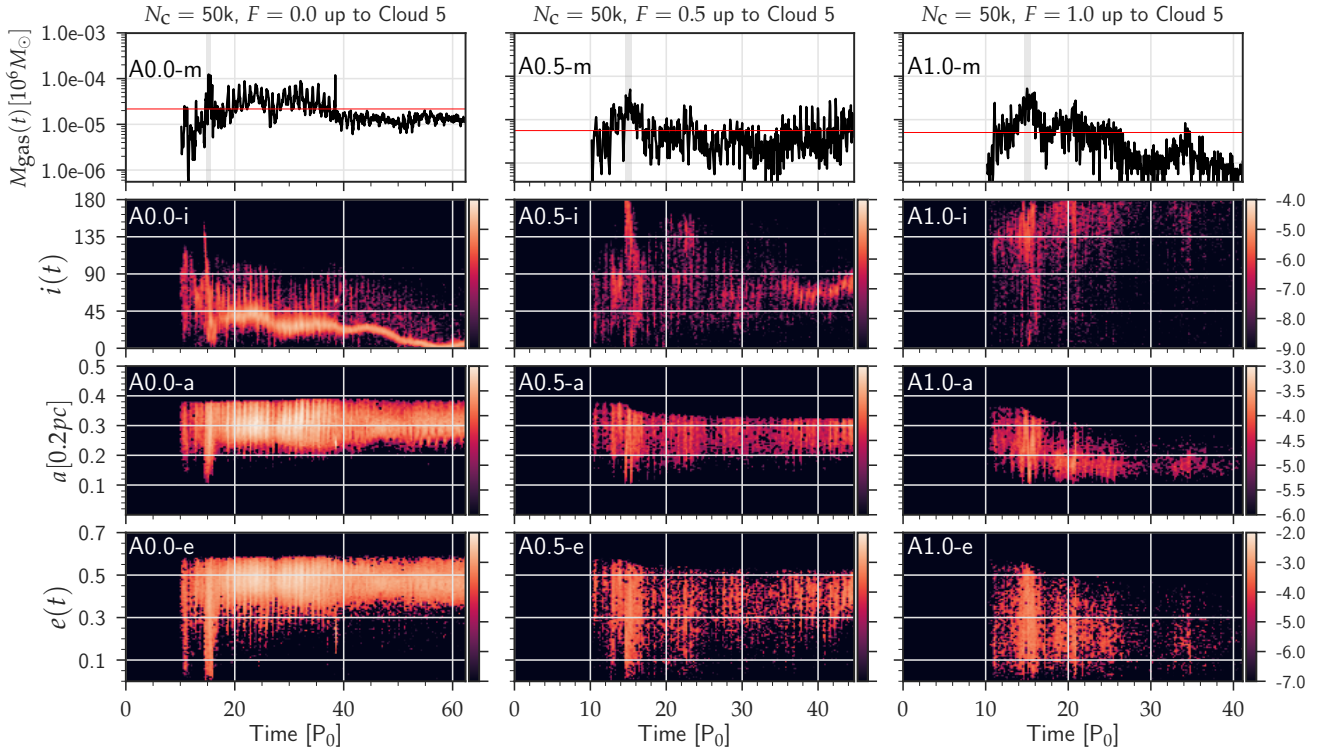


Figure 15. Same as Figure 12 but for the “forked” simulations. Note the log-scale in the top row.

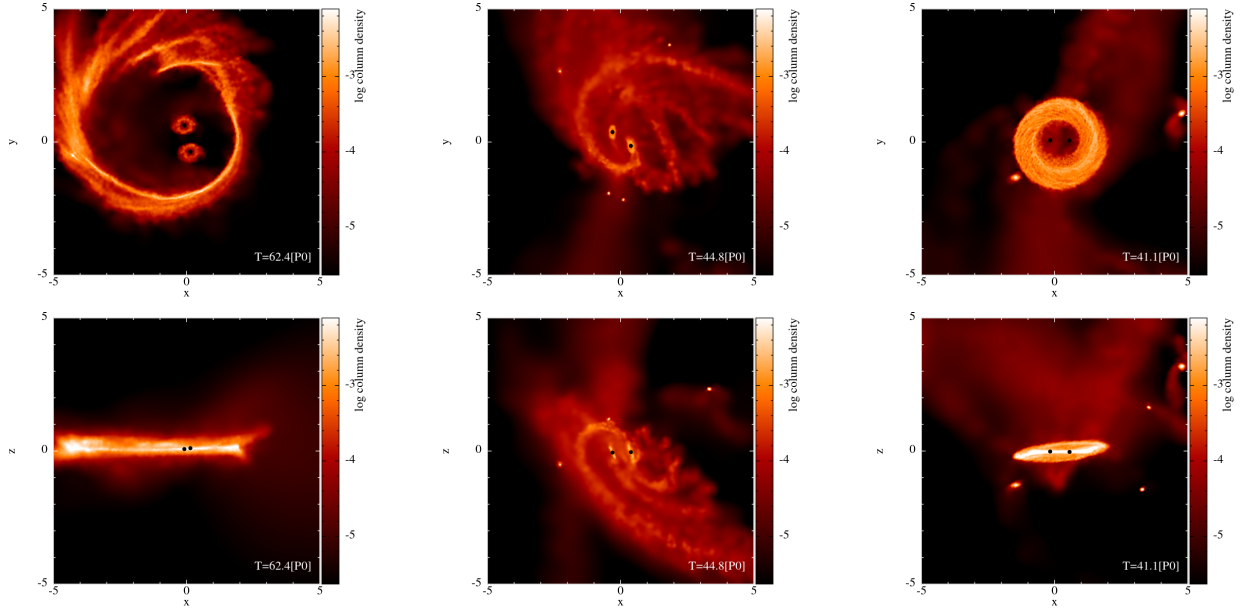


Figure 16. Visualisation of the last snapshot of the “forked” simulations. $F = 0.0$, $F = 0.5$ and $F = 1.0$ runs are shown left to right. The top and bottom row display $x - y$ and $x - z$ views of the system.

cause its partial disruption. Even in the co-rotating simulations ($F = 0.0$), after the addition of 20 clouds, injecting in the system a gas mass equal to 20% of the MBHB mass, the circumbinary disc mass does not exceed a mere 1% of the binary mass ($\approx 10^4$ solar masses for our fiducial system). Extrapolating from Goicovic et al. (2016), the naive expectation would be that about 50% of the injected mass ends up in a circumbinary structure ($\approx 10^5$ solar masses for our fiducial system). More isotropic and counter-rotating cloud distributions ($F = 0.5$ and $F = 1.0$) result in even lighter and more transient circumbinary discs.

Counter-rotating rings. The interaction with counter-rotating gas clouds result in the formation of compact counter-rotating rings. Due to the absence of Lindblad resonances for co-rotating orbits, the inner edge of the ring has about the size of the MBHB orbit and is not sustained by its forcing quadrupolar potential, resulting in an extremely unstable structure. The net consequence is that interaction with clouds on small impact parameters easily disrupt those rings, triggering copious accretion on the MBHB. Therefore, building-up extended counter-rotating structures is virtually impossible in our scenario, since it would require a much more gentle supply of material with larger angular momentum, within a relatively small range of inclinations.

Mini-discs formation. As expected from previous studies (Goicovic et al. 2016), a co-rotating cloud distribution ($F = 0.0$) results in the formation of prominent mini-discs. Although those mini-discs can also be significantly affected by the infall of new clouds, they are usually able to maintain certain stability, and they re-build quite efficiently following disruption from particularly aggressive cloud interactions. There is a notable tendency of the mini-discs to align after a few orbital periods (see, Figure 12). mini-discs are much less prominent in the $F = 0.5$ and $F = 1.0$ runs. Because of the higher relative velocity between the gas particles and the MBHs, the cross section of gas capture within the MBH Roche Lobe is often smaller than the sink radius. It is possible that mini-discs form also in those cases, but on much smaller scales, that cannot be resolved by our current set-up.

Post interaction relaxation. When the supply of gas clouds ceases, the system tends to relax into a configuration that depends on the overall angular momentum distribution of the gas. This was investigated in our “forked” simulations, in which we limited the supply of gas to the 5th cloud. The stopping of cloud infall avoid further disruption of the circumbinary structures, that grow their mass in time, approaching a stable configuration. After about $20P_0$ from the infall of the last cloud, a prominent co-rotating circumbinary disc forms in the $F = 0.0$ case, whereas a well defined compact thin ring forms in the $F = 1.0$ case. The mass in these structures is about 10% of the total mass content of the supplied clouds. Post-infall relaxation does not lead to any well defined structure in the isotropic case $F = 0.0$, and several incoherent streams are still present at the end of the simulation. We speculate that in the long term, interaction within the stream will result in a relatively homogeneous, tenuous gas envelope.

Accretion onto the MBHB. A consequence of the violent interaction between different clouds and the continuous disruption of circumbinary structure is the triggering of the infall of enormous amount of gas onto the MBHs. This has been seen in larger scale simulations of MBH fuelling (Hobbs et al. 2011; Carmona-Loaiza et al. 2015), and in simulations of accretion onto a MBHB due to ‘disk tearing’ (Doğan et al. 2015); the interaction of gas streams coming from different direction cause efficient cancellation of their respective angular momenta, resulting in efficient infall onto the binary. In the test runs presented here, we showed that the associated accretion rate can be as high as $\approx 100\dot{M}_{\text{Edd}}$, when scaled to our fiducial system. This has a strong effect on the dynamics of the binary, which we investigate in detail in a companion paper (Goicovic et al. (2018)).

Most importantly, our results show that the effect of multiple cloud interactions with a MBHB, does not sum-up to the effect of the single clouds taken individually. Cloud-cloud interactions have a fundamental role in shaping the gaseous structures forming around the binary, promoting continuous formation and disruption of circumbinary discs or ring and triggering episodes of enhanced

accretion onto the MBHB. In general, we found that it is difficult to grow extended, massive circumbinary structures. This means that the evolution of the MBHB in this incoherent-feeding scenario is driven mostly by direct gas capture and accretion rather than resonant torques exerted by a circumbinary disc, as we explore in Goicovic et al. (2018). Our simulations are the first to explore in detail this incoherent MBHB feeding scenario. We focused on some specific aspects of the system evolution, but there is a number of different properties of the systems that can be further investigated. For example, the distribution of dense clumps can be used to simulate star cluster formation in the vicinity of the binary and to study their further interaction with the binary. Likewise, the final state of the system can be evolved for longer time to better assess the stability and fate of the gaseous structures on longer timescales. Due to computational constraints, we could follow “forked” simulations only for $20\text{--}25P_0$, corresponding to only 0.2 Myr for our fiducial system. Finally, we remark that we implemented an extremely simplified hydrodynamic scheme, featuring an effective isothermal/adiabatic equation of state and ignoring any feedback from accretion onto the MBHB. Eventually, our result should be tested against enhanced simulations including realistic cooling prescription capturing disc fragmentation, together with a scheme tracing accretion feedback on the surrounding gas.

ACKNOWLEDGEMENTS

The simulations were partially run between the *minerva* cluster at AEI, and the *sandy-bridge* nodes at HITS. CMF acknowledges support from the Transregio 7 “Gravitational Wave Astronomy” financed by the Deutsche Forschungsgemeinschaft DFG (German Research Foundation). CMF acknowledges support from the DFG Project “Supermassive black holes, accretion discs, stellar dynamics and tidal disruptions”, awarded to PAS, and the International Max-Planck Research School. FG acknowledges support from the CONICYT-PCHA Doctorado Nacional scholarship, the ERC-StG grant EXAGAL-308037, and the Klaus Tschira Foundation. AS is supported by the Royal Society. PAS acknowledges support from the Ramón y Cajal Programme of the Ministry of Economy, Industry and Competitiveness of Spain, as well as the COST Action GWverse CA16104. This work has been partially supported by the CAS President’s International Fellowship Initiative.

REFERENCES

- Abramowicz M. A., Czerny B., Lasota J. P., Szuszkiewicz E., 1988, *ApJ*, **332**, 646
- Amaro-Seoane P., Freitag M., Spurzem R., 2004, *MNRAS*, **352**, 655
- Amaro-Seoane P., et al., 2012, *Classical and Quantum Gravity*, **29**, 124016
- Amaro-Seoane P., et al., 2013a, *GW Notes*, Vol. 6, p. 4–110, **6**, 4
- Amaro-Seoane P., Brem P., Cuadra J., 2013b, *ApJ*, **764**, 14
- Amaro-Seoane P., Maureira-Fredes C., Dotti M., Colpi M., 2016, *A&A*, **591**, A114
- Amaro-Seoane P., et al., 2017a, preprint, ([arXiv:1702.00786](https://arxiv.org/abs/1702.00786))
- Amaro-Seoane P., et al., 2017b, preprint, ([arXiv:1702.00786](https://arxiv.org/abs/1702.00786))
- Armitage P. J., Natarajan P., 2005, *ApJ*, **634**, 921
- Artymowicz P., Lubow S. H., 1994, *ApJ*, **421**, 651
- Barnes J., Hut P., 1986, *Nature*, **324**, 446
- Bate M. R., Bonnell I. A., Price N. M., 1995, *MNRAS*, **277**, 362
- Begelman M. C., Blandford R. D., Rees M. J., 1980, *Nature*, **287**, 307
- Berczik P., Merritt D., Spurzem R., Bischof H.-P., 2006, *ApJ*, **642**, L21
- Bonnell I. A., 1994, *MNRAS*, **269**
- Bonnell I. A., Rice W. K. M., 2008, *Science*, **321**, 1060
- Carmona-Loaiza J. M., Colpi M., Dotti M., Valdarnini R., 2015, *MNRAS*, **453**, 1608
- Colpi M., Dotti M., 2011, *Advanced Science Letters*, **4**, 181
- Cuadra J., Armitage P. J., Alexander R. D., Begelman M. C., 2009, *MNRAS*, **393**, 1423
- D’Orazio D. J., Haiman Z., MacFadyen A., 2013a, *MNRAS*, **436**, 2997
- D’Orazio D. J., Haiman Z., MacFadyen A., 2013b, *MNRAS*, **436**, 2997
- Dabringhausen J., Hilker M., Kroupa P., 2008, *MNRAS*, **386**, 864
- Dotti M., Colpi M., Haardt F., 2006, *MNRAS*, **367**, 103
- Dotti M., Volonteri M., Perego A., Colpi M., Ruszkowski M., Haardt F., 2010, *MNRAS*, **402**, 682
- Dotti M., Colpi M., Pallini S., Perego A., Volonteri M., 2013, *ApJ*, **762**, 68
- Doğan S., Nixon C., King A., Price D. J., 2015, *MNRAS*, **449**, 1251
- Dunhill A. C., Alexander R. D., Nixon C. J., King A. R., 2014, *MNRAS*, **445**, 2285
- Eggleton P. P., 1983, *ApJ*, **268**, 368
- Escala A., Larson R. B., Coppi P. S., Mardones D., 2004, *ApJ*, **607**, 765
- Escala A., Larson R. B., Coppi P. S., Mardones D., 2005a, *ApJ*, **630**, 152
- Escala A., Larson R. B., Coppi P. S., Mardones D., 2005b, *ApJ*, **630**, 152
- Ferrarese L., Merritt D., 2000, *ApJ*, **539**, L9
- Frank J., Rees M. J., 1976, *MNRAS*, **176**, 633
- Gallego-Cano E., Schödel R., Dong H., Nogueras-Lara F., Gallego-Calvente A. T., Amaro-Seoane P., Baumgardt H., 2017, preprint, ([arXiv:1701.03816](https://arxiv.org/abs/1701.03816))
- Gaspari M., Ruszkowski M., Oh S. P., 2013, *MNRAS*, **432**, 3401
- Gaspari M., Brighenti F., Temi P., 2015, *A&A*, **579**, A62
- Gaspari M., Temi P., Brighenti F., 2017, *MNRAS*, **466**, 677
- Gebhardt K., et al., 2000, *AJ*, **119**, 1157
- Genzel R., Eisenhauer F., Gillessen S., 2010, *Reviews of Modern Physics*, **82**, 3121
- Goicovic F. G., Cuadra J., Sesana A., Stasyszyn F., Amaro-Seoane P., Tanaka T. L., 2016, *MNRAS*, **455**, 1989
- Goicovic F. G., Sesana A., Cuadra J., Stasyszyn F., 2017, *MNRAS*, **472**, 514
- Goicovic F. G., Maureira-Fredes C., Sesana A., Amaro-Seoane P., Cuadra J., 2018, preprint, ([arXiv:1801.04937](https://arxiv.org/abs/1801.04937))
- Haiman Z., Kocsis B., Menou K., 2009, *ApJ*, **700**, 1952
- Häring N., Rix H.-W., 2004, *ApJ*, **604**, L89
- Hernquist L., 1990, *ApJ*, **356**, 359
- Hobbs A., Nayakshin S., Power C., King A., 2011, *MNRAS*, **413**, 2633
- Khan F. M., Just A., Merritt D., 2011, *ApJ*, **732**, 89
- King A. R., Pringle J. E., 2006, *MNRAS*, **373**, L90
- King A. R., Lubow S. H., Ogilvie G. I., Pringle J. E., 2005a, *MNRAS*, **363**, 49
- King A. R., Lubow S. H., Ogilvie G. I., Pringle J. E., 2005b, *MNRAS*, **363**, 49
- Kocsis B., Haiman Z., Loeb A., 2012a, *MNRAS*, **427**, 2680
- Kocsis B., Haiman Z., Loeb A., 2012b, *MNRAS*, **427**, 2680
- Kormendy J., 2003, in Ho L., ed., “Coevolution of Black Holes and Galaxies”, Carnegie Observatories, Pasadena.
- Kormendy J., Ho L. C., 2013, *ARA&A*, **51**, 511
- Larson R. B., 1981, *MNRAS*, **194**, 809
- MacFadyen A. I., Milosavljević M., 2008, *ApJ*, **672**, 83
- Maccagni F. M., Morganti R., Oosterloo T. A., Oonk J. B. R., Emonts B. H. C., 2018, preprint, ([arXiv:1801.03514](https://arxiv.org/abs/1801.03514))
- Magorrian J., et al., 1998, *AJ*, **115**, 2285
- Merritt D., Milosavljević M., 2005, *Living Reviews in Relativity*, **8**, 8
- Milosavljević M., Merritt D., 2003, *ApJ*, **596**, 860
- Milosavljević M., Merritt D., 2001, *ApJ*, **563**, 34
- Naab T., Burkert A., 2001, in Knapen J. H., Beckman J. E., Shlosman I., Mahoney T. J., eds, *Astronomical Society of the Pacific Conference Series Vol. 249, The Central Kiloparsec of Starbursts and AGN: The La Palma Connection*. p. 735 ([arXiv:astro-ph/0110374](https://arxiv.org/abs/astro-ph/0110374))
- Nixon C., Lubow S. H., 2015, *MNRAS*, **448**, 3472
- Ohsuga K., Mori M., Nakamoto T., Mineshige S., 2005, *ApJ*, **628**, 368
- Perret V., Renaud F., Epinat B., Amram P., Bornaud F., Contini T., Teyssier R., Lambert J.-C., 2014, *A&A*, **562**, A1

- Preto M., Berentzen I., Berczik P., Spurzem R., 2011, *ApJ*, **732**, L26
- Prieto J., Escala A., Volonteri M., Dubois Y., 2017, *ApJ*, **836**, 216
- Quinlan G. D., 1996, *New Astron.*, **1**, 35
- Roedig C., Sesana A., 2014, *MNRAS*, **439**, 3476
- Roedig C., Dotti M., Sesana A., Cuadra J., Colpi M., 2011, *MNRAS*, **415**, 3033
- Sanders D. B., Mirabel I. F., 1996, *ARA&A*, **34**, 749
- Schödel R., Ott T., Genzel R., Eckart A., Mouawad N., Alexander T., 2003, *ApJ*, **596**, 1015
- Schödel R., Feldmeier A., Kunneriath D., Stolovy S., Neumayer N., Amaro-Seoane P., Nishiyama S., 2014, *A&A*, **566**, A47
- Schödel R., Gallego-Cano E., Dong H., Nogueras-Lara F., Gallego-Calvente A. T., Amaro-Seoane P., Baumgardt H., 2017, preprint, ([arXiv:1701.03817](https://arxiv.org/abs/1701.03817))
- Sesana A., Khan F. M., 2015, *MNRAS*, **454**, L66
- Sesana A., Haardt F., Madau P., 2007, *ApJ*, **660**, 546
- Sesana A., Barausse E., Dotti M., Rossi E. M., 2014, *ApJ*, **794**, 104
- Springel V., Hernquist L., 2002, *MNRAS*, **333**, 649
- Tang Y., MacFadyen A., Haiman Z., 2017a, *MNRAS*, **469**, 4258
- Tang Y., MacFadyen A., Haiman Z., 2017b, *MNRAS*, **469**, 4258
- Tombesi F., Sambruna R. M., Reeves J. N., Braito V., Ballo L., Gofford J., Cappi M., Mushotzky R. F., 2010, *ApJ*, **719**, 700
- Tombesi F., Meléndez M., Veilleux S., Reeves J. N., González-Alfonso E., Reynolds C. S., 2015, *Nature*, **519**, 436
- Tremblay G. R., et al., 2016, *Nature*, **534**, 218
- Vasiliev E., Antonini F., Merritt D., 2015, *ApJ*, **810**, 49
- Volonteri M., 2010, *A&ARv*, **18**, 279
- Volonteri M., Haardt F., Madau P., 2003, *ApJ*, **582**, 559

APPENDIX A: GENERATING THE CLOUDS' INITIAL CONDITIONS FROM THE ANGULAR MOMENTUM VECTOR

The initial angular momentum vector of each cloud orbit is determined by sampling the orientation and the pericentre distance. However, the orbit of each cloud is not fully determined, as a Keplerian trajectory is defined by a total of 6 parameters. Having $(\theta_\ell, \phi_\ell, r_p)$, together with the initial distance and speed of the cloud, leaves one degree of freedom, which basically means that we can choose the initial position to be oriented in *any* direction as long as it lies on the plane defined by the unitary vector

$$\hat{\ell} = (\cos \phi_\ell \sin \theta_\ell, \sin \phi_\ell \sin \theta_\ell, \cos \theta_\ell), \quad (\text{A1})$$

where θ_ℓ and ϕ_ℓ are the polar and azimuthal angles of the angular momentum direction, respectively.

The initial position and velocity vectors are generated by first obtaining an arbitrary unitary vector \hat{e} lying on the aforementioned plane by taking the cross product with the x -axis

$$\hat{e} = \hat{\ell} \times \hat{x}. \quad (\text{A2})$$

Then we rotate this vector by a random angle β , drawn uniformly between 0 and 2π , using the expression

$$\mathbf{r}' = \hat{e} \cos \beta + (\hat{\ell} \times \hat{e}) \sin \beta. \quad (\text{A3})$$

This ensures that there is no preferential direction of incoming gas.

On the other hand, the velocity vector also lies on the plane defined by the angular momentum ($\hat{\ell}$), but is rotated by an angle θ_{vel} with respect to the position vector, and therefore it can be obtained using a similar expression

$$\mathbf{v}' = \hat{e} \cos(\beta - \theta_{\text{vel}}) + (\hat{\ell} \times \hat{e}) \sin(\beta - \theta_{\text{vel}}), \quad (\text{A4})$$

where β has the same value as used in eq. (A3). The angle θ_{vel} is

Distribution	Cloud	RunA					RunB						
		$\hat{r}[a_0]$	$\hat{\theta}[a_0]$	$\hat{\phi}[a_0]$	$\hat{v}[a_0]$	$\hat{v}[a_0]$	$\hat{r}[a_0]$	$\hat{\theta}[a_0]$	$\hat{\phi}[a_0]$	$\hat{v}[a_0]$			
$F = 0.0$	01	14.63	1.24	3.04	-0.22	0.09	-0.04	1.68	10.45	-10.63	-0.05	-0.23	0.09
	02	-10.06	5.58	-9.62	0.21	-0.09	-0.15	-11.00	-7.22	-7.21	-0.22	0.10	0.05
	03	-12.28	6.96	-5.08	0.12	-0.14	0.17	-0.38	-8.18	-14.66	-0.02	-0.17	0.18
	04	-4.13	-10.12	10.28	0.06	0.09	-0.22	-10.65	-5.85	-8.80	0.21	0.10	0.09
	05	12.21	7.61	-4.25	-0.22	-0.08	0.07	-13.12	7.25	0.43	0.19	-0.16	0.01
	06	1.54	-7.94	12.63	0.05	0.21	-0.12	-12.88	-0.82	-7.65	0.22	-0.08	0.09
	07	6.10	6.20	-12.22	-0.04	0.00	0.25	-4.80	11.49	8.36	-0.03	-0.15	-0.20
	08	11.08	3.20	9.60	-0.19	0.00	-0.15	6.41	12.84	-4.38	-0.11	-0.22	0.06
	09	10.63	-10.37	-2.10	-0.16	0.19	-0.04	-13.07	-0.03	-7.35	0.18	-0.11	0.14
	10	13.52	4.21	-4.93	-0.22	-0.02	0.12	12.04	8.12	-3.75	-0.24	-0.03	0.05
	11	10.23	10.79	1.97	-0.21	-0.09	-0.07	-5.79	-9.17	-10.36	0.13	0.20	0.08
	12	-1.35	11.93	-8.99	-0.07	-0.23	0.07	-0.85	-14.98	-0.06	0.01	0.22	-0.11
	13	-2.67	-6.03	-13.47	0.14	0.10	0.19	8.24	-5.29	11.36	-0.11	0.11	-0.20
	14	8.18	-1.46	-12.49	-0.09	0.05	0.23	-10.31	-8.45	6.88	0.20	0.15	-0.05
	15	4.68	5.60	13.11	-0.09	0.01	-0.22	6.82	3.50	-12.90	-0.16	-0.03	0.19
	16	—	—	—	—	—	—	-9.59	-10.59	4.56	0.17	0.18	-0.04
	17	—	—	—	—	—	—	-4.74	-12.65	6.52	0.15	0.20	-0.04
	18	—	—	—	—	—	—	-13.91	4.85	2.84	0.20	-0.13	-0.09
	19	—	—	—	—	—	—	-14.41	-3.42	2.38	-0.19	0.05	-0.16
	20	—	—	—	—	—	—	-12.34	-8.50	0.73	0.13	0.21	0.02
$F = 0.5$	01	14.63	1.24	3.04	-0.22	0.09	-0.04	1.68	10.45	-10.63	-0.05	-0.23	0.09
	02	-10.06	10.81	2.62	0.21	-0.09	-0.10	-11.00	0.12	-10.20	0.22	0.04	0.11
	03	-12.28	6.96	-5.08	0.12	-0.14	0.17	-0.38	-8.35	-12.46	-0.02	0.07	0.24
	04	-4.13	-14.40	-0.76	0.06	0.23	-0.08	-10.65	-1.93	-10.39	0.21	0.06	0.12
	05	12.21	-8.52	-1.82	-0.22	0.11	0.02	-13.12	-4.87	-5.39	0.19	0.12	0.10
	06	1.54	-7.94	12.63	0.05	0.21	-0.12	-12.88	-0.82	-7.65	0.22	-0.08	0.09
	07	6.10	11.37	-7.64	-0.04	-0.12	0.22	-4.80	11.49	8.36	-0.03	-0.15	-0.20
	08	11.08	3.20	9.60	-0.19	0.00	-0.15	6.41	12.84	-4.38	-0.11	-0.22	0.06
	09	10.63	-9.54	4.59	-0.16	0.12	-0.14	-13.07	-5.28	5.12	0.18	0.18	-0.02
	10	13.52	4.21	-4.93	-0.22	-0.02	0.12	12.04	8.12	-3.75	-0.24	-0.03	0.05
	11	10.23	10.79	1.97	-0.21	-0.09	-0.07	-5.79	-7.62	-11.55	0.13	0.18	0.11
	12	-1.35	-13.21	-6.97	-0.07	0.16	0.19	-0.85	-14.98	-0.06	0.01	0.22	-0.11
	13	-2.67	5.47	-13.71	0.14	-0.06	0.21	8.24	-5.29	11.36	-0.11	0.11	-0.20
	14	8.18	6.74	-10.61	-0.09	-0.10	0.21	-10.31	-5.12	9.61	0.20	0.11	-0.10
	15	4.68	5.60	13.11	-0.09	0.01	-0.22	6.82	3.50	-12.90	-0.16	-0.03	0.19
	16	-1.93	-13.95	5.17	0.11	0.17	-0.15	-9.59	-10.59	4.56	0.17	0.18	-0.04
	17	12.22	-6.54	-5.73	-0.22	0.12	-0.02	-4.74	-12.65	6.52	0.15	0.20	-0.04
	18	0.21	7.90	-12.75	0.03	-0.02	0.25	-13.91	-4.08	3.86	0.20	0.12	-0.10
	19	2.26	-5.10	13.92	-0.03	0.04	-0.24	-14.41	-3.28	2.56	-0.19	0.04	-0.16
	20	6.53	-8.72	-10.31	-0.15	0.09	0.18	-12.34	7.32	-4.38	0.13	-0.20	0.07
$F = 1.0$	01	14.63	1.24	3.04	-0.22	0.09	-0.04	1.68	1.55	-14.83	-0.05	-0.12	0.21
	02	-10.06	10.81	2.62	0.21	-0.09	-0.10	-11.00	0.12	-10.20	0.22	0.04	0.11
	03	-12.28	-2.25	-8.31	0.12	0.10	0.20	-0.38	-8.35	-12.46	-0.02	0.07	0.24
	04	-4.13	-14.40	-0.76	0.06	0.23	-0.08	-10.65	-1.93	-10.39	0.21	0.06	0.12
	05	12.21	-8.52	-1.82	-0.22	0.11	0.02	-13.12	-4.87	-5.39	0.19	0.12	0.10
	06	1.54	11.66	9.31	0.05	-0.10	-0.21	-12.88	6.29	4.43	0.22	-0.01	0.12
	07	6.10	11.37	-7.64	-0.04	-0.12	0.22	-4.80	-7.31	12.19	-0.03	0.18	-0.17
	08	11.08	-6.62	-7.64	-0.19	0.06	0.15	6.41	1.77	-13.45	-0.11	-0.04	0.22
	09	10.63	-9.54	4.59	-0.16	0.12	-0.14	-13.07	-5.28	5.12	0.18	0.18	-0.02
	10	13.52	3.18	5.66	-0.22	-0.09	-0.06	12.04	-8.91	0.81	-0.24	0.05	-0.04
	11	10.23	-8.59	-6.82	-0.21	0.05	0.12	-5.79	-7.62	-11.55	0.13	0.18	0.11
	12	-1.35	-13.21	-6.97	-0.07	0.16	0.19	-0.85	-13.70	-6.04	0.01	0.25	-0.01
	13	—	—	—	—	—	—	8.24	10.96	6.07	-0.11	-0.19	-0.13
	14	—	—	—	—	—	—	-10.31	-5.12	9.61	0.20	0.11	-0.10
	15	—	—	—	—	—	—	6.82	-7.47	-11.08	-0.16	0.12	0.15
	16	—	—	—	—	—	—	-9.59	8.97	7.25	0.17	0.16	-0.09
	17	—	—	—	—	—	—	-4.74	8.48	11.43	0.15	-0.07	-0.19
	18	—	—	—	—	—	—	-13.91	-4.08	3.86	0.20	0.12	-0.10
	19	—	—	—	—	—	—	-14.41	-3.28	2.56	-0.19	0.04	-0.16
	20	—	—	—	—	—	—	-12.34	-8.50	0.73	0.13	0.21	0.02

Table A1. Initial 3-D position and velocity (x, y, z components) of the centre of mass of each cloud for RunA and RunB.

directly related to the pericentre distance as follows

$$\theta_{\text{vel}} = \arcsin \left(\frac{v_p}{v_{\text{ini}}} \frac{r_p}{d_{\text{ini}}} \right), \quad (\text{A5})$$

where $d_{\text{ini}} = 15a_0$ is the initial distance to the binary centre of mass, $v_{\text{ini}} = 0.25\sqrt{GM_0/a_0}$ is the initial velocity and v_p is the velocity at periaapsis.

Finally, we normalise these vectors to the initial distance and velocity,

$$\mathbf{r} = \frac{d_{\text{ini}}}{\|\mathbf{r}'\|} \mathbf{r}', \quad (\text{A6})$$

$$\mathbf{v} = -\frac{v_{\text{ini}}}{\|\mathbf{v}'\|} \mathbf{v}', \quad (\text{A7})$$

which yields the orbit defined by the sampled angular momentum vector. The initial position and velocity vectors of each cloud are displayed in Table A1, listed here so that the results can be reproduced by future studies.

APPENDIX B: SUPPLEMENTARY SUITE OF SIMULATIONS (RUNC)

We show here some results for the extra suite of simulations (RunC) combining the cloud angular momentum distribution and pericentre distances of RunA (see Figure 3 and 2) with the cloud time of arrivals of RunB (see Table 1). Due to limiting computing

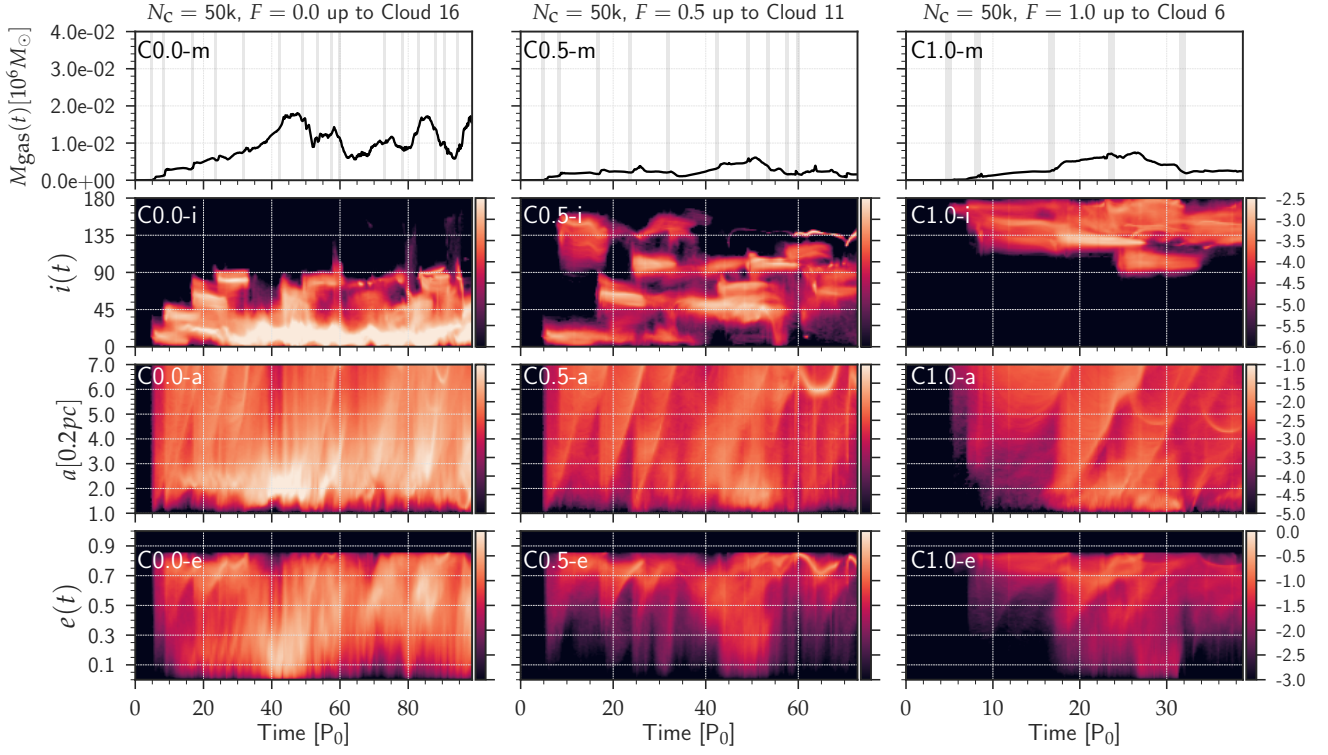


Figure B1. Same as Figure 10 for RunC.

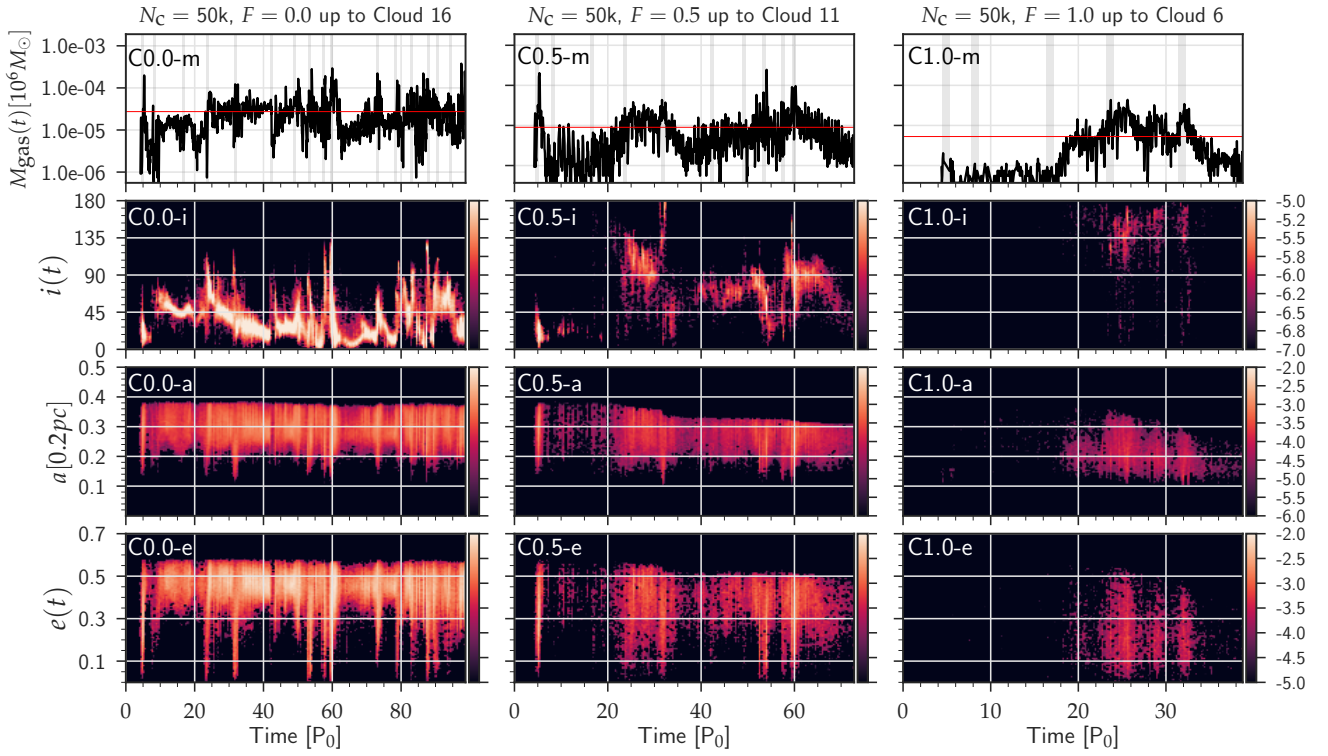


Figure B2. Same as Figure 12 for RunC.

power, only 16 10 and 5 clouds arrived onto the binary in run $F = 0.0$, $F = 0.5$ and $F = 1.0$ respectively. And main properties of the gas structures forming along the simulations are shown in Figure B1 and B2.

The overall behaviour of simulations is quite similar to what shown in Figure 10 and 12 for RunA. Indicating, not surprisingly, that the distribution of the cloud parameters, rather than their times of arrival, leaves a strong imprint on the forming gas structures. The $F = 0.0$ case (left column in both figures) initially builds up a prominent, co-rotating circumbinary structure confined to $i < 30^\circ$ and $a < 3$ (Figure B1), which is partially destroyed by clouds incoming at $T \approx 50P_0$. A similar behaviour is seen in the mini-discs evolution (Figure B2). Note, however that the mini-disc inclination shows much larger fluctuations often reaching values larger than 45° . Mass accumulation in circumbinary structures is much smaller in the $F = 0.5$ and $F = 1.0$ cases (central and right columns, respectively), and mini-discs are much lighter and intermittent (especially in the $F = 1.0$ case), in line with the general finding of RunA and RunB. Overall, this new suite of runs confirm the robustness of the general features highlighted in the main body of the paper.

This paper has been typeset from a \LaTeX file prepared by the author.